~~GROUP 4~~
~~Downgraded at 3-year intervals; declassified after 12 years~~

[redacted]

[redacted]

Copy No. 30

NASA Project Apollo Working Paper No. 1089

APOLLO REENTRY HEATING [U]

(NASA-TM-X-66780) APOLLO REENTRY HEATING N79-76503
(NASA) 65 p

Unclas
00/18 11653

ICATION CHANGE
To UNCLASS
By authority [illegible] Date [illegible]
Changed by [illegible]
Classified Document Master Control Station, NASA
Scientific and Technical Information Facility

FF No. 602(A)

(ACCESSION NUMBER) (THRU)
65 (PAGES) None (CODE)
NASA-TMX-66780 (NASA CR OR TMX OR AD NUMBER) (CATEGORY)

[redacted]

DISTRIBUTION AND REFERENCING

This paper is not suitable for general distribution or referencing. It may be referenced only in other working correspondence and documents by participating organizations.

[redacted]

NATIONAL AERONAUTICS AND SPACE ADMINISTRATION
MANNED SPACECRAFT CENTER
Houston, Texas
September 13, 1963

[redacted]

~~THIS MATERIAL CONTAINS INFORMATION AFFECTING THE NATIONAL DEFENSE OF THE UNITED STATES WITHIN THE MEANING OF THE ESPIONAGE LAWS, TITLE 18, U. S. C., SECS. 793 AND 794, THE TRANSMISSION OR REVELATION OF WHICH IN ANY MANNER TO AN UNAUTHORIZED PERSON IS PROHIBITED BY LAW.~~

CASE FILE COPY

[redacted]

NASA PROJECT APOLLO WORKING PAPER NO. 1089

[U]

APOLLO REENTRY HEATING

Prepared by:

Dorothy B. Lee
STD-Aerodynamics

John J. Bertin
STD-Aerodynamics

Robert C. Ried
STD-Aerodynamics

[redacted]

Authorized for Distribution:

Warren Gillespie, Jr.
for Maxime A. Faget
Assistant Director, Research and Development

NATIONAL AERONAUTICS AND SPACE ADMINISTRATION

MANNED SPACECRAFT CENTER

HOUSTON, TEXAS

SEPTEMBER 13, 1963

[redacted]

TABLE OF CONTENTS

Section Page

SUMMARY 1

INTRODUCTION 1

LIST OF SYMBOLS 2

RESULTS AND DISCUSSION 4

Convective Heating 4
Thermal Air Radiation Encountered During Apollo Reentry . 10
Radiative Heating Distribution About The Apollo Command Module 12
Application Of Heating Rates To Apollo Reentry 17

CONCLUDING REMARKS 18

REFERENCES 20

APPENDIX A

Convective Heating Theory 22

APPENDIX B

Thermal Radiation Characteristics Associated With A Strong Shock In Air 26

TABLE I 31

FIGURES 1 TO 25 . . . . 32 to 59

LIST OF FIGURES

Figure — Page

1 The test conditions for the heat transfer wind tunnel program 32

2 Laminar heat transfer rate distribution in the pitch plane of the reentry configuration at 33° angle of attack 33

3 Experimental pressure distribution in the pitch plane of the entry configuration at 33° angle of attack 34

4 Comparison of experimental and theoretical heat transfer rate distribution in the pitch plane of the reentry configuration at 33° angle of attack . . . 35

5 Heat transfer rate distribution for the reentry configuration at 33° angle of attack 36

6 Heat transfer rate distribution in the pitch plane of the reentry configuration as a function of angle of attack 37

7 Convective heat transfer rate at the stagnation point of the reentry configuration at zero angle of attack 38

8 Heat transfer rate distribution in the pitch plane of the reentry configuration at 33° angle of attack 39

9 Boundary layer trip configuration 40

10 Comparison of heat transfer rate distribution for the spherical heat shield obtained using models with and without boundary layer trip 41

11 Thermal radiation characteristics associated with a strong shock in air 42

(a) Profile of thermal radiation intensity behind a strong shock in air 42

LIST OF FIGURES

Figure Page

(b) Integrated radiation flux toward the body as a function of the distance behind the shock 42

12 Thermal radiation flux to the stagnation point of the Apollo at 33° angle of attack 43

13 Flow regimes experienced by the Apollo at angle of attack as a function of the altitude and the velocity 44

14 Schematic representation of the approximations used to obtain the thermal radiation flux to a general point on the forebody of the Apollo at angle of attack 45

15 Schematic representation of the shock shape in the angle of attack plane for the Apollo 46

16 Measured and assumed relative local shock standoff distance for the forebody of the Apollo at angle of attack 47

17 Relative distribution of thermal radiation flux to the surface of the Apollo at angle of attack 48

18 Distribution of relative thermal radiative heating flux on the forebody of the Apollo at angle of attack 49

19 Heat shield design trajectory envelope 50

20 Time histories of theoretical convective stagnation point heating rates at $\alpha=0°$ 51

(a) For trajectories HSE-1, HSE-3A, and HSE-4A . . . 51

(b) For trajectories HSE-2 and HSE-6 52

[redacted]

LIST OF FIGURES

Figure Page

21 Time histories of theoretical radiative stagnation point heating rates when $\alpha=33°$ 53

(a) For trajectories HSE-1, HSE-2, and HSE-3A 53

(b) For trajectories HSE-4A and HSE-6 54

22 Distribution of heat load for two design trajectories 55

(a) For overshoot trajectory, HSE-3A 55

(b) For emergency reentry trajectory HSE-6 56

23 Heating rates at location of maximum heating 57

24 Temperature distribution near insulated wall 58

25 Temperature distribution near a non-insulated cold wall 59

[redacted]

APOLLO REENTRY HEATING

SUMMARY

Calculations of heating rates have been made on the Apollo Command Module based on theory and experimental data measured in various tunnel facilities. Convective and radiative heating rates have been estimated for the heat shield design trajectories proposed by North American Aviation. A distribution of convective heating around the Command Module obtained from the tunnel data measured in the laminar flow regime is presented. Calculations of radiation intensity were applied to obtain time histories of radiative rates and radiative distributions on the Command Module.

INTRODUCTION

Convective heating rates have been measured around the Apollo Command Module shape with the configuration at angle of attack in various tunnel facilities. The purpose of this paper is to present the latest heating estimates for the Apollo reentry configuration based on tunnel measurements and theory. This paper supersedes the working paper of reference 1.

The distribution obtained from tunnel measurements and a laminar stagnation point theory have been used to estimate the convective heating that the Apollo vehicle will experience at flight conditions encountered during the proposed reentry trajectories. Tunnel test data that are discussed also include measurements that were presented in references 2 and 3.

Estimates of the radiative heating rates are based on theory normalized by shock tube measurements. The estimates are considered conservative but until more experimental data are available it is necessary to take a conservative approach.

Two appendixes are also included to further explain the convective theories and the fundamentals of thermal radiation.

LIST OF SYMBOLS

A	reference area, 129 sq ft
C	non-equilibrium radiation flux, watts/cu cm
C_D	drag coefficient
c_p	specific heat of air at constant pressure, Btu/lb-R°
D	drag, lb and maximum body diameter
E	radiation intensity, watts/cu cm
E_B	equilibrium radiation intensity at body, watts/cu cm
E_{BS}	equilibrium radiation intensity behind shock, watts/cu cm
E_q	equilibrium radiation intensity, watts/cu cm
G	load factor
h	enthalpy, Btu/lb
h_D	dissociation enthalpy
k	thermal conductivity, (Btu)(ft)/(sq ft)(sec)(°R)
Le	Lewis number
L	lift, lb
M	Mach number
N_{Pr}	Prandtl number
p	pressure, lb/sq ft
p	distance along streamline
$\dot{q}$	heating rate, Btu/(sq ft) (sec)
Q	total heating, Btu/sq ft

r_o	radius of cross section of body of revolution
R	maximum body radius, 6.4167 ft
R	universal gas constant
Re	Reynolds number
R'	radius of curvature, ft
S	distance along surface from center of spherical heat shield, ft
T	temperature, °R
t	time, sec
U	velocity, ft/sec
U_N	velocity component normal to shock, ft/sec
W	weight, lb
x	distance along surface from angle-of-attack stagnation point, ft
x_N	distance normal to body from shock, cm
x_S	stagnation point standoff distance, cm
y	distance normal to the surface, ft
α	angle of attack, deg
β	angle between shock normal and body normal, deg
γ	reentry angle, deg
Δ	relaxation distance along streamline
δ_1	distance to peak non-equilibrium intensity, cm
δ_2	length of non-equilibrium region to 110% of equilibrium intensity, cm
ϵ	ρ_1/ρ_∞

η_r	recovery factor
μ	absolute viscosity, slugs/ft-sec
ρ	density, slugs/cu ft
ϕ	angle between pitch plane and any plane containing the axis of symmetry, deg

Subscripts:

1	behind shock
c.o.	circular orbit
D	diameter
e	entry
eff	effective
r	recovery
S.L.	sea level
t	stagnation
W	wall
l	local
∞	free stream

RESULTS AND DISCUSSION

Convective Heating

Tunnel facilities.- To determine the convective heating experienced by an Apollo capsule upon reentry, an extensive wind tunnel program has been undertaken. The range of flow conditions tested in the program are presented in figure 1 in terms of the free stream Mach number and the Reynolds number, based on free stream conditions and the maximum body diameter. As a result of the low free stream static temperatures in the wind tunnel, the tunnel conditions have no meaning in the velocity-altitude coordinate system.

The extreme flight conditions that might be experienced by the Apollo capsule upon reentry are indicated in figure 1 by the HSE-3A overshoot trajectory and the HSE-6, 20G emergency reentry trajectory. Either the velocity-altitude coordinate system or the Mach number—Reynolds number coordinate system may be used to designate a given flight condition for these trajectories.

Heat transfer rates have been measured in various facilities for the reentry configuration over an extensive angle of attack range at free stream Mach numbers from 6 to 20 with free stream Reynolds numbers in the range 30,000 to 6,780,000. A 0.02 scale model of the Apollo reentry configuration has been tested in the Jet Propulsion Laboratory 21-inch Hypersonic Wind Tunnel for Mach numbers from 6 to 9 over a range of Reynolds numbers from 60,000 to 806,000. A 0.045 scale model has been tested in the Arnold Engineering Development Center Tunnel C (AEDC) at a nominal Mach number of 10 over a range of Reynolds numbers from 190,000 to 1,400,000. Tests have been performed in the Cornell Aeronautical Laboratory 48-inch Hypersonic Shock Tunnel for Mach numbers from 6 to 17.3 with Reynolds numbers ranging from 30,000 to 6,780,000 using a 0.05 scale model. A 0.04 scale model has been tested in Tunnel F at the Arnold Engineering Development Center at a nominal Mach number of 20 and a Reynolds number of 65,000. In each case the test gas was air.

Laminar heat transfer.- The data obtained in the experimental program have been nondimensionalized by dividing the local heat transfer rate measured when the model is at angle of attack by the heat transfer rate measured at the stagnation point when the model is at zero angle of attack. The distributions are presented as a function of the nondimensionalized surface coordinate, S/R, which is the surface distance from the center of the spherical heat shield divided by the maximum body radius. The maximum body radius for the full scale Apollo is 77 inches. With the data presented in this manner, essentially one distribution was obtained for all test conditions with the exception of the test performed in CAL's 48-inch Hypersonic Shock Tunnel at a Reynolds number of 6,780,000 and a Mach number of 6.38, which may have experienced turbulent flow. The results of this test will be discussed in a later section.

The heating rate distribution in the pitch plane, that is, the plane of symmetry, is presented in figure 2 for the reentry configuration at an angle of attack of 33°. Five points of interest are: (1) the geometric center of the spherical heat shield, S/R of 0.00, (2) the actual stagnation point for the configuration at 33° angle of attack, S/R from 0.79 to 0.88, (3) the geometric stagnation point for the configuration at 33° angle of attack, S/R of 0.982, (4) the point of maximum heating, S/R approximately 0.98, and (5) the maximum body radius, S/R of 1.08. The maximum heat transfer rate was found to occur approximately two-thirds of a foot from the location of the maximum body radius toward the geometric center, when measured on a full scale Apollo.

The pressure distribution in the pitch plane of the reentry configuration at 33° angle of attack is presented in figure 3 as the ratio of the local static pressure to the stagnation pressure behind the shock. The solid curve of figure 3 represents a fairing of the data. The experimental pressure data indicate that the stagnation point is located between S/R = 0.79 and S/R = 0.88. The location is approximately 20° from the axis of symmetry when measured by the spherical heat shield radius. As the density ratio, ρ_1/ρ_∞, is increased, the actual stagnation point will move toward the geometric stagnation point.

The method of Lester Lees (ref. 4) has been used to predict the ratio of the local heat transfer rate in the pitch plane of the reentry configuration at 33° angle of attack to the heat transfer rate at the stagnation point of the reentry configuration at zero angle of attack. The fluid properties were determined using the perfect gas relations of the Ames Tables (ref. 5) and the experimental pressure distribution given by the curve of figure 3. The theoretical heat transfer rate distribution predicted by Lees' method, which is valid for laminar flow, is compared in figure 4 with the experimental distribution measured at JPL at a Mach number of 9.07 with a Reynolds number of 175,500. The theoretical distribution is in very good agreement with the experimental data.

The theoretical distribution of figure 4 is the ratio of the local heating rate for the reentry configuration at 33° angle of attack to the heating rate at the stagnation point of the configuration at zero angle of attack. The curve represents Lees' equation (ref. 4) in the form:

$$\frac{\dot{q}}{\dot{q}_{t,\alpha=0^\circ}} = \left[\frac{U_\infty}{2^{k_s+1}\left(\frac{dU_l}{dS}\right)_{t,\alpha=0^\circ}}\right]^{\frac{1}{2}} \left\{\frac{\frac{p_l}{p_t}\left(\frac{\mu_l}{\mu_t}\frac{T_t}{T_l}\right)\left(\frac{U_l}{U_\infty}\right) r_o^{k_b}}{\left[\int_o^x \frac{p}{p_t}\left(\frac{\mu_l}{\mu_t}\frac{T_t}{T_l}\right)\left(\frac{U_l}{U_\infty}\right) r_o^{2k_b} dx\right]^{\frac{1}{2}}}\right\}_{\alpha=33^\circ} \qquad (1)$$

(A brief explanation of the equations related to convective heat transfer is given in Appendix A).

The exponents, k_s and k_b, in equation (1) account for the geometry of the flow. For axisymmetric flow the exponents assume a value of unity and for planar flow the exponents are zero. Since the flow over the reentry configuration at zero angle of attack is axisymmetric, k_s was chosen to be unity. Oil flow photographs indicate that flow in the pitch plane of the reentry configuration at 33° angle of attack approximates two-dimensional, or planar, flow. Therefore, zero was used as the value for k_b.

The distance x is measured along the body surface from the measured stagnation point of the configuration at 33° angle of attack. The distance S is measured along the body surface from the geometric center of the spherical heat shield, which is the stagnation point of the configuration at zero angle of attack.

Since Lees' equation for the heating rate distribution is indeterminate at the angle of attack stagnation point, S/R approximately 0.8, the heat transfer rate distribution in this region merely represents a fairing of the results obtained on either side of the stagnation point. It should be noted that the maximum heat transfer rate does not occur at the stagnation point, but on the shoulder of the capsule, S/R approximately 0.98.

Lines of constant heat transfer rate are presented in figure 5 for the reentry configuration at 33° angle of attack. The distributions represent a fairing of data measured in Tunnel C at a nominal Mach number of 10 with Reynolds numbers from 190,000 to 1,400,000. The instrumentation locations are indicated by the crosses of figure 5. The forebody data are presented as an azimuthal equidistant projection centered on the geometric center of the spherical heat shield. The geometric center of the apex of the conical portion of the capsule was chosen as the center of the afterbody data.

Since the models were supported in the tunnel by means of a sting on the leeward side, data could not be obtained in the pitch plane on the leeward afterbody. However, data have been obtained at the Ames Research Center's One-foot Hypervelocity Shock Tunnel by George Fox (ref. 6) on an Apollo-like capsule supported by a sting brought out the apex. The data indicate heat transfer rates in the pitch plane on the leeward afterbody to be approximately one percent of the heat transfer rates at the stagnation point of the reentry configuration at zero angle of attack.

Although the current nominal trim angle is 33°, the possibility exists that an angle of attack variation of ± 4° will occur during reentry. Presented in figure 6 are heating rate distributions in the pitch plane measured at a Mach number of 10.17 with a Reynolds number of 918,900 for angles of attack from 28° to 35°. The heating rates on the leeward side of the vehicle vary inversely with the angle of attack, while the heating rates on the windward side vary directly.

In order to substantiate the validity of the wind tunnel data, for each test the theoretical heat transfer rate at the stagnation point of the configuration at zero angle of attack was compared with the experimental value. This comparison is presented in table I for the data obtained on a 0.02 scale model, designated H-1, which was tested at Jet Propulsion Lab (JPL) and at AEDC, and on a 0.045 scale model, designated H-2, tested at AEDC. The laminar stagnation point theory of Fay and Riddell (ref. 7) which was used to predict the heat transfer rate for the configuration at zero angle of attack, agrees within ± 15 percent for most of the measurement. The heat transfer rate can be expressed by this theory as:

$$\dot{q}_{t,\alpha=0^\circ} = 0.76\left(N_{Pr}\right)^{-0.6}\left(\rho_w\mu_w\right)^{0.1}\left(\rho_t\mu_t\right)^{0.4}\left(h_t-h_w\right)\sqrt{\left(\frac{dU_l}{dS}\right)_{t,\alpha=0^\circ}} \qquad (2)$$

For a modified Newtonian flow, the square root of the velocity gradient is:

$$\sqrt{\left(\frac{dU_l}{dS}\right)_{t,\alpha=0^\circ}} = 1.06\left[\frac{1}{R'}\sqrt{\frac{2\left(p_t - p_\infty\right)}{\rho_t}}\right]^{\frac{1}{2}} \qquad (3)$$

where 1.06 is the ratio of the heat transfer rate at the stagnation point of an Apollo reentry configuration at zero angle of attack to the heat transfer rate to a hemisphere of radius equal to the radius of the spherical heat shield of the Apollo according to Stoney (ref. 8).

For convenience the theoretical convective heat transfer rate at the stagnation point of the Apollo reentry configuration at zero angle of attack is presented as a function of velocity and altitude in figure 7. Included are the extreme flight conditions likely to be experienced by the Apollo Command Module upon reentry indicated by the overshoot trajectory and the 20G emergency return trajectory. Figure 7 may be used with figure 5 to determine the local heating rate at any point on the Apollo vehicle at 33° angle of attack. The maximum, zero angle of attack, stagnation point heat transfer rate upon reentry of the Apollo configuration, which occurs during the emergency return trajectory, was found to be 283 Btu/ft^{2}sec. To determine this theoretical heating rate, the equation of Detra, Kemp, and Riddell (ref. 9) was used in the form:

$$\dot{q}_{t,\alpha=0^\circ} = 1.06 \left\{ \frac{17,600}{\sqrt{R'}} \left(\frac{\rho_\infty}{\rho_{s-L}}\right)^{0.5} \left(\frac{U_\infty}{U_{c.o.}}\right)^{3.15} \right\} \qquad (4)$$

where 1.06 is the Stoney factor and R', the radius of the spherical heat shield, is 184.8 inches. Equation (4), which differs from equation (2) by less than five percent for free stream velocities up to 36,000 feet per second, was used due to the simplicity of calculation.

Turbulent heat transfer.- As mentioned previously, a single test showed a deviation from the laminar heat transfer distribution. This distribution, compared in figure 8 with the average experimental laminar distribution, was measured at a Reynolds number of 6,780,000 with a Mach number of 6.38 in the Cornell Aeronautical Laboratory's 48-inch Shock Tunnel. The data are presented as the ratio of the local heating rate measured for the model at 33° angle of attack to the heating rate measured at the stagnation point at zero angle of attack. However, since the measured value of the zero angle of attack stagnation point heat transfer rate was found to be approximately twice the theoretical prediction, the values of the nondimensionalized heat transfer rates are very questionable. It is significant that the heating rates measured away from the stagnation region are significantly higher than the laminar rates, indicating that transition of the flow to turbulent may have occurred. Additional wind tunnel data necessary to define the transition Reynolds number are not available at this time.

Surface roughness.- Some experimental data are available to determine the effect of surface roughness. Boundary layer trips consisting of four rows of $\frac{1}{32}$ -inch steel balls, spaced $\frac{1}{16}$ -inch apart, were spot welded to a 0.045 scale model, as shown in figure 9. Heat transfer data were obtained at a nominal Mach number of 10 for free stream Reynolds numbers, based on the model diameter, of 570,000 and 1,380,000. The heating rate distributions obtained using the roughened model are compared in figure 10 with the distributions measured on a smooth model at the same nominal test conditions. The data obtained at the higher Reynolds number showed a significant increase in the heating rates downstream of the trips. However, the distribution measured at the lower Reynolds number agrees closely with the distribution obtained using a smooth model except in the immediate vicinity of the boundary layer trips.

Experimental data summarized by Braslow (ref. 10) indicate that, for three dimensional roughness particles, transition to turbulence occurs when $\sqrt{Re_k}$ is approximately 20. The Reynolds number, Re_k, is based on the roughness height and the local properties at the top of the roughness. For the test conducted at the lower free stream Reynolds number, $\sqrt{Re_k}$ was found to be 12.95, while at the higher free stream Reynolds number, $\sqrt{Re_k}$ was 23. Thus, the increase in heating downstream of the trips for the higher Reynolds number case was apparently the result of transition of the flow to turbulent flow. However, it did not maintain turbulence and therefore is not characteristic of natural transition.

Since the influence of roughness on transition is considerably smaller in compressible than in incompressible flow, similar beads spot welded on the afterbody had no effect on the heat transfer rate distribution along the conical generator parallel to the free stream flow.

On the full size Apollo vehicle, these beads would correspond to roughness particles 0.695 inch in diameter (approximately $\frac{11}{16}$ inch). At present it is thought that the actual surface roughness will be much less than the 0.695 inch simulated for these tests. Therefore, although local increases in the heat transfer rate may be experienced, the surface roughness will have only a minor effect on transition.

Thermal Air Radiation Encountered During Apollo Reentry

The thermal air radiation flux to a point on a body is the sum or integral of all the radiation intensity in the gas cap, directed toward that point. An accurate determination of the radiation flux to a given point requires a knowledge of the distribution of radiation intensity within the gas cap. In the Apollo flight regime, the intensity of thermal radiation from air at a given thermodynamic and chemical state is known only within a factor of two. The state of the air at a general point in the gas cap of the Apollo Command Module is not known since the flow field about an asymmetric body has not as yet been solved. Conservative estimates of the radiative heating to the Apollo Command Module may be obtained by the use of a few reasonable assumptions and experimental data obtained for the Apollo configuration.

Stagnation point radiative heating for a blunt body.- The radiative flux in the immediate vicinity of the stagnation point on a blunt body may be approximated by a one-dimensional analysis. This is done by assumming that the body and the shock are two parallel planes separated by a finite gas cap thickness, or shock standoff distance. For this approximation the radiative flux to the stagnation point is equal to one-half of the integral of the radiation intensity profile between the shock wave and the body. The remaining half of the radiation flux is emitted in a direction away from the body. This approximation is slightly conservative since for a convex shock the radiation intensity profile decreases with distance away from the stagnation point.

The profile of the thermal radiation intensity behind a strong shock in air has been determined experimentally (ref. 11) and is shown schematically in figure 11(a). The intensity of radiation exhibits a non-equilibrium overshoot behind a strong shock, where the air is in a chemical and thermodynamic non-equilibrium reaction to the shock wave. As the air relaxes to equilibrium, the intensity of radiation relaxes to the corresponding equilibrium value. A more detailed explanation of the thermal radiation characteristics associated with a strong shock in air is given in Appendix B.

Various aspects of the thermal radiation profile have been determined experimentally as a function of velocity and density level. For convenience, these results have been approximated by empirical relations.

The integrated non-equilibrium radiation flux toward the body is a function of velocity only (ref. 11) and has been approximated by the relation:

$$C = e^{(2.17 \times 10^{-4} U_\infty - 3.563)} \tag{5}$$

The intensity of equilibrium radiation has been assumed to be that which is radiated from air at stagnation point conditions. The analytical and experimental results of Kivel and Bailey (ref. 12) have been applied to the stagnation conditions obtained by using the free-stream conditions of the ARDC 1959 atmosphere (ref. 13) and may be approximated by the relation:

$$\log_{10} E_q = \frac{\log_{10} \frac{\rho_\infty}{\rho_{S.L.}} - 8.41\, e^{-6.25 \times 10^{-5} U_\infty}}{0.734 - 4.45 \times 10^{-6} U_\infty} - \frac{5.6\, e^{-(U_\infty - 2.6 \times 10^{4})^{2} (1.538 \times 10^{-8})} + 5.5}{0.734 - 4.45 \times 10^{-6} U_\infty} \tag{6}$$

The distance behind the shock to the peak of the overshoot intensity and the distance to the point where the radiation intensity has reduced from the overshoot value to 110 percent of the equilibrium radiation, have been measured experimentally (ref. 11) and are approximated respectively by the following relations:

$$\log_{10} \delta_1 = 4.24\, e^{-7.25\times 10^{-5} U_\infty} - 1.0204 \log_{10} \left(\frac{\rho_\infty}{\rho_{S.L.}} \right) - 4.76 \tag{7}$$

$$\log_{10} \delta_2 = 8.435\, e^{-7\times 10^{-5} U_\infty} + 14.545\, e^{-2.45\times 10^{-4} U_\infty} - 1.0204 \log_{10} \left(\frac{\rho_\infty}{\rho_{S.L.}} \right) - 4.77 \tag{8}$$

The intensity profile, E (P), behind a strong shock in air has been approximated by an empirical relation exhibiting an exponential overshoot with a relaxation to equilibrium:

$$E(P) = E_q + \left\{ \frac{2 E_q^2 P(P-\delta_1)}{\delta_1 \left[C+E_q (\delta_1-\delta_2) \right]} + \frac{PC}{\delta_1^2} + E_q \left(\frac{2P}{\delta_1} - \frac{\delta_2 P}{\delta_1^2} + \frac{P^2}{\delta_1^2} - 1 \right) \right\} e^{-\frac{P^2}{2\delta_1^2} \left[\frac{2\delta_1 E_q}{C+E_q(\delta_1-\delta_2)} + 1 \right]} \tag{9}$$

This relation is subject to the constraints of C, EQ, δ_1 and δ_2 as a function of U_∞ and $\frac{\rho_\infty}{\rho_{S.L.}}$. The intensity profile may then be integrated in closed form with respect to the distance behind the shock wave. This gives the radiation flux to the stagnation point as a function of the standoff distance. The stagnation point radiation flux to a blunt body is shown schematically in figure 11 (b) and may be expressed in the form:

$$\dot{q}_t = \int_0^{x_S} E(P)\, dP = 0.88 \left\{ E_q x_S + C - E_q \delta_2 \right\} \left\{ 1 - e^{-\frac{x_S^2}{2\delta_1^2} \left[\frac{2\delta_1 E_q}{C+E_q} (\delta_1-\delta_2) + 1 \right]} \right\} \tag{10}$$

Apollo shock standoff distance at the stagnation point.- To apply these results for the prediction of the radiation flux to the stagnation point of a particular blunt reentry vehicle, the stagnation point standoff distance must be known as a function of velocity and altitude. The available data for the Apollo at angle of attack indicates that the stagnation point standoff distance behaves in about the same manner as a sphere with an effective radius given by:

$$R_{eff} \cong 0.55\ D \tag{11}$$

The empirical relation for the stagnation point standoff distance of a sphere, used for these radiation calculations is a modified form of a relation developed by Li and Geiger (ref. 14):

$$\frac{R_{eff}}{x_S} = \frac{(\epsilon - 1)^2}{\epsilon - \sqrt{2\epsilon - 1}} - 1 \tag{12}$$

Thus for the Apollo at 33° angle of attack, the standoff distance of the shock wave at the stagnation point is given by:

$$x_S = \frac{0.55\ D}{\dfrac{(\epsilon - 1)^2}{\epsilon - \sqrt{2\epsilon - 1}} - 1} \tag{13}$$

where D is the body diameter in cm.

Radiative flux to the Apollo stagnation point.- The relations (5) through (13) determine the stagnation point radiative heat flux to the Apollo at 33° angle of attack for any velocity, altitude combination. Figure 12 illustrates lines of constant stagnation point radiative heating flux as a function of velocity and altitude for the Apollo configuration at angle of attack. The values shown in figure 12 are not significantly more conservative than the equilibrium radiation values obtained from Kivel and Bailey (ref. 12).

Radiative Heating Distribution About The Apollo Command Module

To determine the radiation flux to a general point on the Apollo Command Module, it is necessary to assume either a shock shape and a radiation intensity distribution or a shock shape and a distribution of gas properties within the gas cap. In either case the general characteristics of the flow in the regions of interest must be investigated.

Flow regimes of interest.- Figure 13 is an altitude-velocity plot which shows the various flow regimes and includes three of the NAA lunar return design trajectories. The region of interest is defined as the region where the stagnation point radiation flux for the Apollo configuration at 33° angle of attack exceeds 1.0 Btu/ft^2-sec, as shown in this figure. In the low altitutde, or high density regime the gas cap flow is primarily in chemical and thermodynamic equilibrium with the exception of a very narrow band of non-equilibrium flow immediately behind the shock. In figure 13 the shaded region designated as equilibrium flow, is the regime where the non-equilibrium flow behind the normal shock extends through less than 10 percent of the standoff distance.

In the high altitude, or low density region, the non-equilibrium flow extends through a much longer time or distance behind the shock. The shaded region of figure 13, designated as non-equilibrium flow, is a region where the non-equilibrium flow distance behind the normal shock is at least as great as the stagnation point standoff distance. The intermediate region of mixed non-equilibrium and equilibrium flow has been defined merely to separate the two extreme regions.

Radiation intensity within the gas cap.- For the equilibrium flow, and the non-equilibrium and equilibrium flow regions, the intensity of equilibrium radiation adjacent to any point on the vehicle may be readily calculated. The pressure distribution over the forebody may be obtained by experimental measurement such as shown in figure 3. If the air adjacent to the body is assumed to have expanded isentropically from the stagnation point, the local pressure determines the thermodynamic and chemical state of the air at that point. The intensity of equilibrium radiation at the body (E_B) may then be calculated or obtained from radiation tables of air (ref. 12).

The equilibrium air state behind the shock may be obtained by the equations of motion and the properties of air at equilibrium. The intensity of equilibrium radiation behind the shock (E_{BS}) may again be obtained from Kivel and Bailey (ref. 12). In the equilibrium flow regime, it is a good approximation to assume that this equilibrium intensity behind the shock occurs immediately behind the non-equilibrium region. This assumption breaks down as the non-equilibrium relaxation distance increases. In the non-equilibrium flow regime this intensity, E_{BS}, is not obtained since the gas has expanded by the time equilibrium is reached as shown in figure 14. For the three lunar return trajectories considered the peak radiative heating rates correspond to relatively short non-equilibrium relaxation distances.

To obtain a distribution of equilibrium radiation intensity within the gas cap, it was first assumed that the enthalpy and entropy varied linearily between the body and the shock. This resulted in an almost linear distribution of radiation intensity across the gas cap. To simplify the calculations, a linear distribution of radiation intensity in a radial direction between the body and the shock was assumed. The assumed radiation intensity distribution is shown schematically in figure 14 for a general point on the forebody. Since the equilibrium radiation intensity depends very strongly on the temperature $(E \sim T^{8} \rightarrow T^{12})$, the assumption of a linear equilibrium radiation intensity profile is far more conservative than the profile obtained by the assumption of a linear temperature across the gas cap.

The non-equilibrium relaxation distance, δ_2, may be obtained at a general point behind the shock by using the normal shock velocity component in equation (8). The relaxation distance normal to the body, $\delta_2/\cos\beta$, was assumed to be the same as δ_2. The thermal radiation flux, C, from this non-equilibrium region may be obtained by inserting the normal velocity component in equation (5). It was assumed that this flux was emitted from a region lying along a normal to the body as shown in figure 14. As indicated in the figure, the validity of this assumption decreases with altitude.

Shock shape in the angle-of-attack plane.- To obtain an estimate of the shock shape about the Apollo Command Module at flight conditions, the measured shock shape, from wind tunnel schlierens, in the angle-of-attack plane, was adjusted with the density ratio across the normal shock. The shock shape measured at $M = 13.1$ and a normal shock density ratio of 5.83 is illustrated in figure 15. The local shock standoff distance normal to the body was divided by the stagnation point standoff distance. This ratio was assumed to be constant for all flight conditions of interest and is shown in figure 16. The stagnation point standoff distance at flight conditions was obtained from equation 13.

Shock shape about the forebody.- The standoff distance, normal to the body and in the plane of $\phi = 90^\circ$, was assumed to be constant over the forebody as shown in figure 16. The standoff distance at a general point on the forebody was assumed to have a value between that of the standoff distance at the 90° plane and that of the standoff distance at the same S/R location in the angle-of-attack plane. The weighting factor for this difference was assumed to be cos ϕ:

$$\left(\frac{x_N}{x_S}\right)_{\frac{S}{R},\,\phi} = \left(\frac{x_N}{x_S}\right)_{S/R,\,\phi=90^\circ} + \cos\phi\left[\left(\frac{x_N}{x_S}\right)_{S/R,\,\phi=0} - \left(\frac{x_N}{x_S}\right)_{S/R,\,\phi=90^\circ}\right], \quad -90^\circ \le \Phi \le 90^\circ \tag{14}$$

Although this shock shape is purely an approximation, it in principle includes the measured data in the angle-of-attack plane as an adjustment to assuming that the shock has the same shape as the body.

Radiation flux distribution.- The assumed radiation intensity distribution within the gas cap has been shown schematically in figure 14. To obtain a distribution of the radiation flux to the body, a one-dimensional analysis was used. It was assumed that one half of the radiation intensity, from a slug of air normal to the body, was emitted toward the body. Although this is a rough approximation, it is felt that it is a good indication of the relative radiation flux to a point on the forebody as compared to the stagnation point flux.

Figure 17 illustrates the relative distribution of radiation flux to the surface, in the angle-of-attack plane, for relatively high radiative heating times encountered during the NAA HSE-3A overshoot and the NAA HSE-6 emergency entry design trajectories.

The approximations used to obtain these radial flux distributions are more accurate for the HSE-6 trajectory than for the HSE-3A trajectory. A more accurate representation of the HSE-3A distribution would conform more closely to that of the HSE-6 distribution for the relatively high radiative heating points on the body. With this in mind it was felt that the distribution of radiative heating encountered during the high heating portion of the HSE-6 trajectory would be indicative of the radiative heating distribution experienced by the Apollo Command Module during significant radiative heating conditions.

Thus, by using the approximations mentioned above, a distribution of radiative heating on the forebody of the Apollo at angle of attack may be obtained. This relative distribution is shown on a polar plot of the surface in figure 18.

Thermal radiation to the afterbody.- In general the predicted thermal radiation intensity from the air adjacent to the afterbody of the Apollo is orders of magnitude below the corresponding stagnation point radiation intensity. Preliminary estimates of the afterbody thermal radiation flux that would occur during the highest level of radiation heating for the HSE-6 trajectory, indicate that the level of this radiation will be negligible. This highest level of radiation heating however, is due to the high density level encountered during the HSE-6 trajectory. For this high density level, the air is essentially in equilibrium as it expands from the forebody gas cap to the afterbody flow. It is possible for this expansion to be chemically and thermodynamically frozen during the lower density level of the HSE-3A, overshoot trajectory. During a frozen expansion, the internal modes of vibration and electronic excitation might not reduce significantly. This might result in a greater flux of radiation to the afterbody than would be encountered during the high density emergency reentry trajectory. A further explanation of this phenomenon is given in Appendix B.

Preliminary calculations as to the low density level required to create this situation indicate that when it occurs the overall thermal radiation level is insignificant. The complete dismissal of this problem cannot be made however, until further fundamental analytical and experimental studies of chemical and physical properties of air and thermal air radiation are made. Of equal importance is the requirement for obtaining an accurate representation of the flow in the afterbody region. This supersonic afterbody flow requires an extremely accurate knowledge of the forebody subsonic gas cap flow.

Application of Heating Rates To Apollo Reentry

Trajectories.- The enclosures of reference 15 present time histories of the revised trajectories proposed by NAA for heat shield design analyses. These trajectories, as shown in figure 19, represent the extreme conditions the Apollo Command Module would experience during earth atmospheric reentry from orbital and lunar flights. They are based upon a Command Module weight of 9,500 pounds, a trim L/D of 0.5 and $\frac{W}{C_D A}$ = 75.0 lb/sq ft with A = 129.0 sq ft for the body diameter of 154 inches.

The HSE-1 and HSE-2 trajectories are entry from orbital flight both having a velocity of 26,000 ft/sec at 400×10^3 feet altitude. The HSE-1 trajectory would result in the configuration experiencing the maximum heat load while the HSE-2 return would produce the maximum heat rates.

The three trajectories reentering from the lunar mission all have a velocity of 36,200 ft/sec at 400×10^3 feet altitude. The HSE-3A or overshoot trajectory would result in the maximum heat load and is described by NAA as having the maximum supercircular speed heat load combined with the maximum subcircular speed heat load. The HSE-4A or undershoot trajectory, which takes the same time to reenter as HSE-3A, has the maximum supercircular speed heat rate combined with the maximum subcircular speed heat load however, the skip out to 464×10^3 feet altitude at 24,600 ft/sec velocity reduces the total heat load by reducing the time that significant heating rates are experienced. The HSE-6 is the 20G emergency reentry trajectory and is designated the structural limit for the design of the Command Module since the highest heating rates would be experienced during this trajectory.

Convective heating rates.- The convective heating rates around the Command Module have been calculated for the trajectories proposed by NAA with the use of a laminar stagnation point theory and the distributions measured in the tunnel. The distribution is presented as a percentage of the stagnation point heating of the configuration at zero angle of attack since this value can be determined theoretically with a large degree of reliability. There are several laminar stagnation point heat transfer theories that have been verified with experimental values measured in free flight up to 15,100 ft/sec velocity. These theories agree within ten to fifteen percent of each other up to 36,000 ft/sec and therefore all are considered applicable for design purposes, even though their validity has not been demonstrated by direct flight tests at the higher speeds. Time histories of $\dot{q}_{t,\alpha=0}$ for each of the design trajectories are shown in figure 20 based on the curve fitting equation of Detra, Kemp and Riddell's theory for a hemisphere (ref. 9) and modified for the Apollo spherical heat shield shape. Local convective heating rates can then be determined for pertinent locations with the use of figure 20 and the distribution presented in figure 5 or figure 8 which shows a fairing of all the laminar data obtained from tunnel measurements.

Radiative heating rates.- Time histories of the 33° trim angle-of-attack stagnation point radiative rates for each of the design trajectories were computed with the use of equation (10) and are shown in figure 21. The local radiative heating rates can then be calculated with the use of figure 21 and the distribution presented in figure 17.

The integrated heating rates with respect to time, or total heat load, are presented in figure 22 for the overshoot trajectory and the emergency reentry trajectory for both the convective and the radiative heating. This comparison shows the contribution of each type of heating plus the summation of both in order to localize the maximum heat load.

Time histories of the convective and radiative heating rates that will occur near the corner of the heat shield where the maximum heating will be experienced are shown in figure 23 for two of the trajectories to demonstrate the magnitude of the two types of heating rates. The convective heating at this corner location was determined from the distribution presented in figure 5 multiplied by the Detra, Kemp and Riddell's theory (ref. 9) for the stagnation point at $\alpha = 0^\circ$. North American Aviation has taken an admittedly conservative approach in calculating the heating at the corner by assuming a two-dimensional body with a radius of 7.7 inches. This estimate would result in the heating at the corner being approximately 3 times the heating at the stagnation point when $\alpha = 0^\circ$ instead of 1.9 as determined by the average of all of the tunnel measurements.

CONCLUDING REMARKS

Measurements of convective heat transfer have been made on scaled models of the Apollo Command Module at various angles of attack in several tunnel facilities. The free stream Mach number range varied from 6 to 20 and free stream Reynolds numbers based on body diameter from 0.03×10^6 to 6.78×10^6.

The measured laminar data agreed very well with theoretical values for heat transfer distributions over blunt-nosed bodies when measured at Reynolds numbers up to 1.4×10^6. One test made at a Reynolds number of 6.78×10^6 resulted in measurements being twice the average experimental laminar distribution. Only the HSE-6 emergency reentry trajectory is in a high Reynolds number regime (approximately 3.0×10^6) and the total heat load based on these high measurements would still be less than that of the HSE-3A overshoot trajectory.

The radiative heating rates to the Apollo reentry configuration are based on conservative estimates and shock-tube measurements of thermal radiation intensity behind a strong shock in air. The chemical and thermodynamic state of the air at any given point in the gas cap between the shock and the body is not known since the flow field about an asymmetric body has not been solved. The assumptions that were made to predict the thermal radiation are considered reasonable but on the conservative side. The complexity of the radiation flux to a body necessitates a conservative approach until further experimental studies are made.

REFERENCES

1. Weston, Kenneth C., Higgins, Peter W. and Ried, Robert C.: Some Calculations of the Reentry Environment of the Apollo Command Module. NASA Project Apollo Working Paper No. 1046, June 5, 1962.

2. Bertin, John J.: A Study of Heat Transfer and Pressure Data Obtained on the 0.02 Apollo Model in the Jet Propulsion Laboratory 21-Inch Hypersonic Wind Tunnel. NASA Project Apollo Working Paper No. 1053, Oct. 3, 1962.

3. Bertin, John J.: A Study of the Heat Transfer Data Obtained on the 0.045 Apollo Model in the Mach 10 Tunnel C at the Arnold Engineering Development Center. NASA Project Apollo Working Paper No. 1067, Feb. 8, 1963.

4. Lees, Lester: Laminar Heat Transfer Over Blunt-Nosed Bodies at Hypersonic Flight Speeds. Jet Propulsion, vol. 26, no. 4, April 1956, pp. 259-269, 274.

5. Ames Research Staff: Equations, Tables, and Charts for Compressible Flow. NACA Report 1135, 1953. (Supersedes NACA TN 1428.)

6. Fox, G.: Convective Heat Transfer to the Apollo Configuration in the Ames 1-Foot Hypervelocity Shock Tunnel. Correspondence transmitted from Ames Research Center to the Manned Spacecraft Center on January 29, 1963.

7. Fay, J. A., and Riddell, F. R.: Theory of Stagnation Point Heat Transfer in Dissociated Air. Jour. Aero. Sci., vol. 25, no. 2, Feb. 1958, pp. 73-85, 121.

8. Stoney, William E., Jr.: Aerodynamic Heating of Blunt Nose Shapes at Mach Numbers Up To 14. NACA RM L58E05a, 1958.

9. Detra, R. W., Kemp, N. H., and Riddell, F. R.: Addendum to Heat Transfer to Satellite Vehicles Re-entering the Atmosphere. Jet Propulsion, vol. 27, no. 12, Dec. 1957, pp. 1256-1257.

10. Braslow, A.: Review of the Effect of Distributed Surface Roughness on Boundary-Layer Transition. AGARD Report 254, April 1960.

11. Study of Thermal Radiation Associated With Non-Equilibrium Flow in the Apollo Flight Regime. Avco-Everett Res. Lab., Final Comprehensive Rpt., Contract NAS 9-156, NASA-MSC, Sept. 1962.

12. Kivel, B. and Bailey, K.: Tables of Radiation from High Temperature Air. Avco-Everett Res. Lab., Res. Rpt. 21, Dec. 1957.

13. Minzner, R. A., Champion, K. S. W. and Pond, H. L.: The ARDC Model Atmosphere. 1959, AFCRC-TR-59-267, Aug. 1959.

14. Li, Ting-Yi and Geiger, Richard E.: Stagnation Point of a Blunt Body in Hypersonic Flow. Jour. Aero. Sci., Jan. 1959.

15. NAA Memo FT/PT/62-135, dtd Aug. 16, 1962, Subject: Atmospheric Exit and Entry Heatshield Design Trajectories.

16. Schlichting, H.: Boundary Layer Theory. McGraw-Hill Book Company, New York, 1960.

17. Shapiro, A.: The Dynamics and Thermo Dynamics of Compressible Fluid Flow. vol. 2, Ronald Press Co., New York, 1954.

18. Kemp, N. H., Rose, P. H., and Detra, R. W.: Laminar Heat Transfer Around Blunt Bodies in Dissociated Air. Journal of the Aerospace Sciences, vol. 26, no. 7, July 1959, pp. 421-430.

19. Fay, J. A., Riddell, F. R., and Kemp, N. H.: Stagnation Point Heat Transfer in Dissociated Air Flow. Jet Propulsion, vol. 27, no. 6, June 1957, pp. 672-674.

APPENDIX A

CONVECTIVE HEATING THEORY

As the gas passes through the shock wave ahead of a blunt body, most of the kinetic energy associated with hypersonic flight speeds is converted to thermal energy and chemical energy. Hence, as a result of the dissociated atoms of nitrogen and oxygen present in the boundary layer, heat transfer to the body surface is accomplished by the energy released during recombination as well as by ordinary heat conduction.

In the limiting case of local thermodynamic equilibrium, the atom concentration vanishes close to the surface, provided the surface temperature is below the dissociation limit at the local pressure. For this case the rate of heat transfer to a unit surface area is given by Fourier's law of heat conduction:

$$\dot{q} = k \left(\frac{\partial T}{\partial y}\right)_{y=0} \tag{A1}$$

where k is the thermal conductivity of the air adjacent to the surface. Whether heat is transferred to or from the surface determines the sign of the air temperature gradient normal to the surface.

A knowledge of the flow field (ref. 16 and 17) is necessary to determine the temperature gradient normal to the wall. For practical purposes viscous and heat conduction effects may be thought of as being confined to a thin boundary layer adjacent to the surface. Outside the boundary layer, viscous forces are negligible compared with the inertial forces, and flow is considered to be isentropic.

Viscous deceleration of the gas in the boundary layer to zero velocity at the wall converts the kinetic energy to thermal energy. If the gas were decelerated adiabatically to zero velocity, the temperature of the gas would rise to the stagnation temperature of the fluid external to the boundary layer. As a result of heat convection away from the surface, the deceleration is non adiabatic and the wall temperature at the wall never reaches the local stagnation temperature. The wall temperature attained is that temperature at which an equilibrium is established between the rate of heat input by frictional dissipation and the rate of heat convection away from an insulated wall (fig. 24). This "adiabatic wall temperature" or "recovery temperature" is related to the stagnation temperature by the recovery factor, η_r ,

$$\eta_r = \frac{T_r - T_l}{T_t - T_l} \tag{A2}$$

For laminar flow the recovery factor is equal to the square root of the Prandtl number and is less than or equal to one.

For the case of a noninsulated wall having a surface temperature, T_w, less than the recovery temperature, the temperature profile is that of figure 25. The maximum temperature attained in the boundary layer is less than the recovery temperature, as a result of heat being transferred toward the surface as well as away from the surface.

Hence, any theoretical analysis of convective heat transfer involves the solution of the fundamental equations governing the motion of a viscous fluid, that is, the Navier-Stokes equations in conjunction with the principles of conservation of energy and conservation of mass. An analytical solution of these equations is extremely complex and laborious, if not impossible, even for basic geometric shapes and boundary conditions. Simplifying assumptions based on a physical understanding of the flow are made to provide useful engineering answers.

Lester Lees has investigated heat transfer to a blunt body having a cold wall based on the following simplying assumptions: (1) the flow is laminar, (2) the local pressure does not vary normal to the surface, (3) the surface is cold relative to the fluid, (4) thermodynamic equilibrium exists, and (5) $\rho_w \mu_w$ is equal to $\rho_l \mu_l$. Lees developed equation (A1) in the form:

$$\dot{q} = 0.50 \left(N_{Pr}\right)^{-0.67} h_t \frac{p_l \left(\frac{\mu_l}{RT_l}\right) U_l r_o^{k_b}}{\left[2\int_0^x p_l \left(\frac{\mu_l}{RT_l}\right) U_l r_o^{2k_b} d_x\right]^{\frac{1}{2}}} \qquad \text{(A3)}$$

which estimates the local heat transfer rate to the Apollo reentry vehicle at 33° angle of attack.

Equation (A1) in the form:

$$\dot{q}_{t,\alpha=0} = 0.50 \sqrt{2^{k_s}} \left(N_{Pr}\right)^{-0.67} \sqrt{\rho_t \mu_t}\, h_t \sqrt{\left(\frac{dU_l}{ds}\right)_{t,\alpha=0^\circ}} \qquad \text{(A4)}$$

approximates the heat transfer rate at the stagnation point of the reentry configuration at zero angle of attack. Equation (A3) has been divided by equation (A4) to present the nondimensional heat transfer rate distribution of equation (1). Kemp, Rose, and Detra (ref. 18) indicated that, even though equation (1) was in good agreement with distributions obtained by more rigorous treatment, equation (A4) should not be used to predict the heating level, because of the simplifying assumptions made.

Oil flow studies indicate that the flow over the reentry configurations at zero angle of attack is axisymmetric, while in the pitch plane of the reentry configuration at 33° angle of attack flow approximates two dimensional flow. Hence, k_b was chosen to be zero, the value of two dimensional flow, and k_s was chosen to be one, the value for flow past a body of revolution. Equation (A4) can be written as:

$$\dot{q}_{t,\alpha=0^\circ} = 0.707\,(N_{Pr})^{-0.67}\sqrt{\rho_t\mu_t}\;h_t\sqrt{\left(\frac{dU_l}{dS}\right)_{t,\alpha=0^\circ}} \qquad \text{(A5)}$$

Boundary layer equations and transformations of the variables similar to those used by Lees were solved numerically by Fay and Riddell. The heat transfer rate at the stagnation point of the reentry configuration at zero angle of attack was found to be:

$$\dot{q}_{t,\alpha=0^\circ} = 0.763\,(N_{Pr})^{-0.60}\sqrt{\rho_t\mu_t}\;(h_t-h_w)\sqrt{\left(\frac{dU_l}{dS}\right)_{t,\alpha=0^\circ}} \quad \text{X}$$

$$\left(\frac{\rho_w\mu_w}{\rho_t\mu_t}\right)^{0.1}\left[1+(Le^{0.52}-1)\,\frac{h_D}{h_t}\right] \qquad \text{(A6)}$$

For hypersonic flow conditions the essential difference between the equation of Fay and Riddell and that of Lees is the product

$$\left(\frac{\rho_w\mu_w}{\rho_t\mu_t}\right)^{0.1}\left[1+(Le^{0.52}-1)\,\frac{h_D}{h_t}\right]$$

As a result of the difficulties involved in determining the Lewis number and the average dissociation energy, the Lewis number, was chosen to be one, reducing the Lewis number factor to unity. Kemp, Rose, and Detra found the Lewis number factor to be 1.078 for $Le = 1.4$ and thermodynamic equilibrium. Fay, Riddell, and Kemp (ref. 19) found that the $\left(\frac{\rho_w\,\mu_w}{\rho_t\,\mu_t}\right)^{0.1}$ term affected the heat transfer rate by as much as seventeen percent for a Lewis number of unity.

The velocity gradient at the stagnation point was determined by solving the incompressible Bernoulli equation for the velocity:

$$U = \sqrt{\frac{2\ p_t}{\rho_t}\left(1 - \frac{p}{p_t}\right)} \qquad \text{(A7)}$$

The modified Newtonian pressure relation for a sphere,

$$\frac{p}{p_t} = \cos^2 \theta + \frac{p_\infty}{p_t} \sin^2 \theta$$

where θ is the angle between the free stream flow and a normal to the surface, was substituted into equation (A7). The velocity was then differentiated with respect to the surface coordinate resulting in the expression.

$$\left(\frac{dU_l}{dS}\right)_{t,\alpha=0^\circ} = \frac{1}{R'}\sqrt{\frac{2\ (p_t - p_\infty)}{\rho_t}} \qquad \text{(A8)}$$

This result was then modified by Stoney's factor (ref. 8) relating the heat transfer rate at the stagnation point of an Apollo reentry configuration at zero angle of attack to the heat transfer rate to a hemisphere of radius equal to the radius of the spherical heat shield of the Apollo vehicle, giving equation (3).

The equation of Detra, Kemp, and Riddell, equation (4), is the result of an empirical approach. Stagnation point heat transfer rates computed by equation (4) differ by less than four percent with stagnation point heat transfer rates predicted by the equation of Fay and Riddell up to velocities of 36,000 feet per second.

APPENDIX B

THERMAL RADIATION CHARACTERISTICS ASSOCIATED WITH A STRONG SHOCK IN AIR

Thermal Radiation

Thermal radiation is a flux of energy traveling in electromagnetic waves. This energy flux is emitted or absorbed primarily by changes in the energy states of electrons. The wavelength of the radiation is inversely proportional to the energy change of the electron. The intensity of the radiation at a given wavelength, is directly proportional to the number of electrons undergoing that corresponding energy change.

If the electron is bound to an atom or molecule, the electron cannot be considered as an entity, but rather it is an intimate part of that unit. Thus, the emission or absorption of a quantum of radiation by an atom or molecule becomes a change in the electronic energy mode of that unit.

The energy states of an atom are limited to the random translational energy and the energy of the electrons relative to the atom. The thermal radiation from an atom or an atomic ion occurs at discrete wavelengths, characteristic of the energy and angular momentum states of the electronic mode of the atom. The discreteness of atomic line radiation is reduced slightly by broadening effects such as the random translational energy of the atom.

The energy states of a molecule or molecular ion include the energy distributions within the modes of vibration, rotation, electronic excitation and random translational energy. Molecular radiation is characterized by a spread throughout a band of wavelengths since one electron transition can result in any of a variety of energies emitted, depending on the relative energy distributed throughout the various modes.

A third source of thermal radiation in a gas is obtained by the scattering of free electrons by ions or neutral particles and the recombination of electrons with ions. Since the kinetic energy of the electrons may have a continuous distribution and the degree of scattering is also continuous, the thermal radiation from free electrons, Kramers radiation, may occur at any wavelength.

To obtain the spectral distribution of radiation intensity emitted from an atom, molecule or a collision it is necessary to assume various basic physical properties of the atom or molecule. Thus for a given energy level the relative probability of emission at various wavelengths may be calculated. The level of radiation must be obtained from experiment. Experimental measurements, however, indicate the validity of the original assumptions. Combined experimental and analytical thermal radiation studies enable the determination of not only the magnitude of the radiation but also the physical and chemical properties of the species being studied.

The radiation characteristics of a given particle depend upon the energy state of the particle and the number and type of collisions it experiences. Thus a prediction of thermal radiation from a gas involves a statistical calculation of the number of particles in a given energy state and the number of specific interactions. Again, experimental measurement can substantiate the statistical analysis. Experimental measurements of thermal radiation from high temperature gases, however, often result in the discovery of new phenomena which are not of significant importance at lower temperatures.

Thermal Radiation From a Non-Equilibrium Gas

If a gas is in a chemical and thermodynamic non-equilibrium state, the thermal radiation characteristics may be significantly different from those of the same gas, with the same energy, at equilibrium. A non-equilibrium gas state may be obtained by a rapid expansion of the gas or by a strong shock wave. In either case the non-equilibrium state is achieved only because there have not been sufficient collisions to maintain equilibrium in a given period of time.

The non-equilibrium expansion or frozen flow, is primarily a function of the pressure or density level. As the gas expands the rate of expansion becomes greater than the chemical and thermodynamic reaction rates. Thus the energy in the internal degrees of freedom, and the energy that would be released if the gas was reacting chemically, is frozen within the gas.

If a gas experiences a strong shock wave, the energy of the flow upstream of the shock is converted primarily into internal energy by the shock wave. The shock wave is a pressure discontinuity which occurs within a few mean-free paths of the gas. In the case of a hypersonic flight situation the free-stream gas is at a relatively low temperature and pressure. It may be characterized as an ideal gas composed of molecules without significant energy in vibration or the electronic degrees of freedom. Behind the shock, however, the gas must become a high temperature, dissociated, ionized, vibrating and electronically excited gas. Although the gas can change pressure instaniously due to the discontinuity in the number of molecules present it cannot react chemically and thermodynamically in a small instant of time.

As a result the free stream gas maintains its identity as it is shocked and results in an extremely high temperature immediately behind the shock, since the energy has not been dissipated into the previously inert degrees of freedom. This high temperature is characteristic of a very high random translational and rotational energy.

To obtain a feeling for this phenomenon it is perhaps better to consider the chemical non-equilibrium aspects alone. If the gas maintained equilibrium at all times, the free-stream molecular gas would have to become dissociated within the thickness of the shock wave. To achieve this, the chemical reaction rates would have to be infinite. This is not the case, however, for either the chemical or the thermodynamic reaction rates.

For the flight conditions of interest, however, the thermodynamic reaction rates are more rapid than the chemical reaction rates. As a result, the hypersonic non-equilibrium transition region in air is characterized by molecules with extremely high energy in all modes. As the air approaches equilibrium, much of this energy is absorbed by the dissociation of these molecules.

This non-equilibrium transition region was first discovered experimentally by the overshoot in the thermal radiation coming from this region. The profile of the thermal radiation behind a strong shock has been illustrated schematically in figure 11(a).

Immediately behind the shock the radiation is negligible since all of the energy is in the form of random translation and rotation. As the air approaches equilibrium a portion of the energy is absorbed by the electronic modes and the thermal radiation approaches a relatively high value. This value reduces, however, as the internal energy is absorbed by the chemical dissociation of the gas. Eventually the gas comes to equilibrium and accordingly the radiation approaches equilibrium.

The chemistry and thermodynamics of the non-equilibrium region are complicated by the complete coupling of almost all of the reaction rates. Because of this coupling and the very nature of the non-equilibrium gas states, there does not appear to be any simple relation between the non-equilibrium radiation and the equilibrium radiation occurring behind the same normal shock. Experimentally, however, it has been determined that in the region of interest the integrated intensity, or flux, of non-equilibrium radiation may be approximated as being independent of the density level. This is due to observations which indicate that the extent of the non-equilibrium region is inversely proportional to the density level while the magnitude of the peak non-equilibrium intensity is proportional to the density level.

If the non-equilibrium radiation intensity profile is approximated by a triangle, the area of the triangle becomes the non-equilibrium radiation flux. The product of the non-equilibrium peak intensity and the relaxation distance is independent of the density level. Thus the non-equilibrium radiation flux is independent of the density level and is a function of velocity only.

Although the non-equilibrium radiation behind a normal shock is fixed by the shock velocity, the non-equilibrium radiation flux to a hypersonic reentry body does depend on the altitude, or density level, as well as the velocity. At high altitudes the vehicle may truncate the non-equilibrium flow. Due to the low density level the non-equilibrium relaxation distance may exceed the normal shock standoff distance. The process may be thought of as the body moving into the non-equilibrium radiation profile. In the severe case the flow will be compressed and then expanded around the body before the peak non-equilibrium radiation may be reached.

At low altitudes the relaxation distance behind a shock is very small compared with the shock standoff distance of a blunt body. Although the non-equilibrium peak intensity can be an order of magnitude greater than the equilibrium intensity, the radiation flux to the body may be dominated by the equilibrium. This is illustrated in sketch (a) where the intensity profile between the shock and the body is shown.

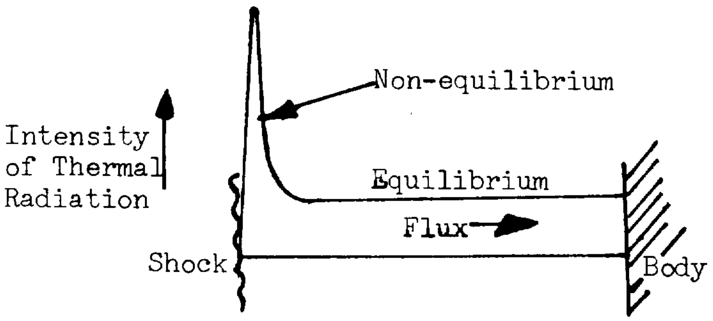

Sketch (a)

The area under this intensity curve is proportional to the flux to the body.

There is one other phenomenon which reduces thermal radiation from a gas at low density. This phenomenon has been termed collision limiting. It is obtained when there are not enough collisions to maintain a population of molecules or atoms with energy in the electronic mode. Thus the energy of the gas is not maintained in a state where it may be radiated away.

It is to be noted that in air the equilibrium radiation intensity has a stronger velocity dependence than the peak non-equilibrium intensity. Thus at reentry velocities in excess of 45,000 feet per second, the equilibrium radiation intensity begins to approach the peak non-equilibrium intensity. In other words, it appears that the equilibrium radiation engulfs the non-equilibrium radiation.

TABLE 1.- WIND TUNNEL MEASUREMENTS COMPARED WITH THEORETICAL VALUES OF $\dot{q}_{t,\alpha=0}$

MODEL	M_∞	Re_D ($\times 10^{-6}$)	$P_{t,\infty}$ (psia)	T_t (°R)	T_w (°R)	$\dot{q}_{meas}$	$\dot{q}_{theory}$	$\frac{\dot{q}_{meas}}{\dot{q}_{theory}}$
H-1	5.99	0.0733	39.3	1562	500	4.71	5.45	.864
H-1	6.10	0.6122	168.0	977	505	3.98	4.47	.890
H-1	6.09	0.7643	168.0	845	498	2.81	3.22	.873
H-1	7.22	0.0726	63.5	1585	506	4.32	4.71	.917
H-1	7.42	0.2859	264.8	1568	515	8.07	8.79	.918
H-1	7.35	0.7569	390.0	1078	504	4.95	5.59	.886
H-1	8.83	0.0596	97.0	1665	501	3.62	4.27	.848
H-1	9.07	0.1761	309.0	1668	505	6.95	7.01	.991
H-1	9.07	0.4595	655	1451	502	7.40	7.90	.937
H-2	10.19	1.3965	1998	1897	720	10.89	9.10	1.197
H-2	10.18	1.1376	1596	1873	691	9.35	8.15	1.147
H-2	10.17	0.9521	1287	1862	686	8.10	7.42	1.092
H-2	10.13	0.5749	753	1801	636	5.80	5.57	1.041
H-2	10.05	0.2240	262	1702	586	3.18	3.16	1.006
H-1	10.13	0.2507	756	1824	589	8.236	8.75	.941
H-1	10.17	0.4066	1293	1878	600	11.372	11.90	.956
H-1	10.18	0.5134	1652	1893	613	13.298	13.50	.985
H-1	10.19	0.6185	2005	1904	624	14.907	14.88	1.002

[redacted]

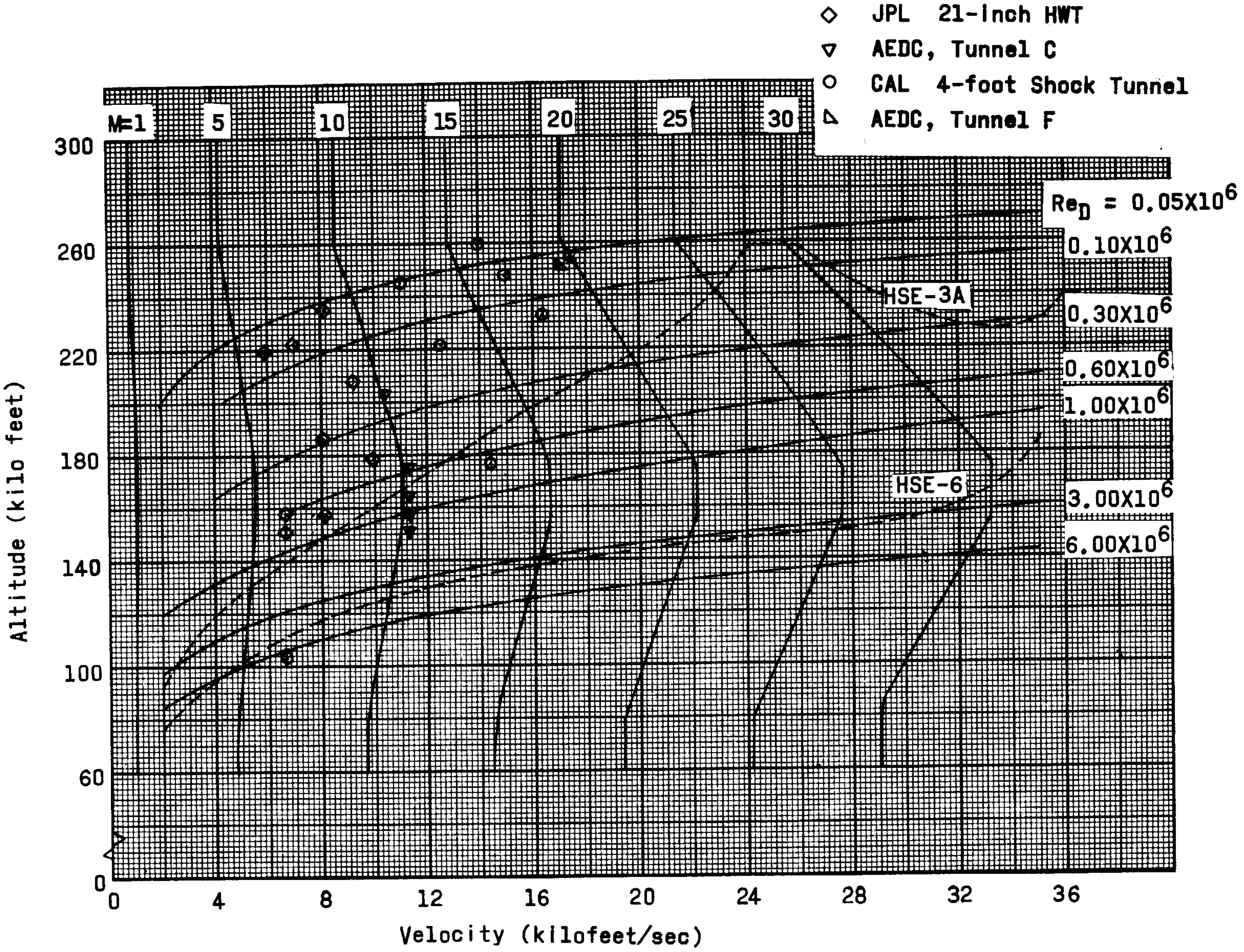

Figure 1.- The test conditions for the heat transfer wind tunnel program.

[redacted]

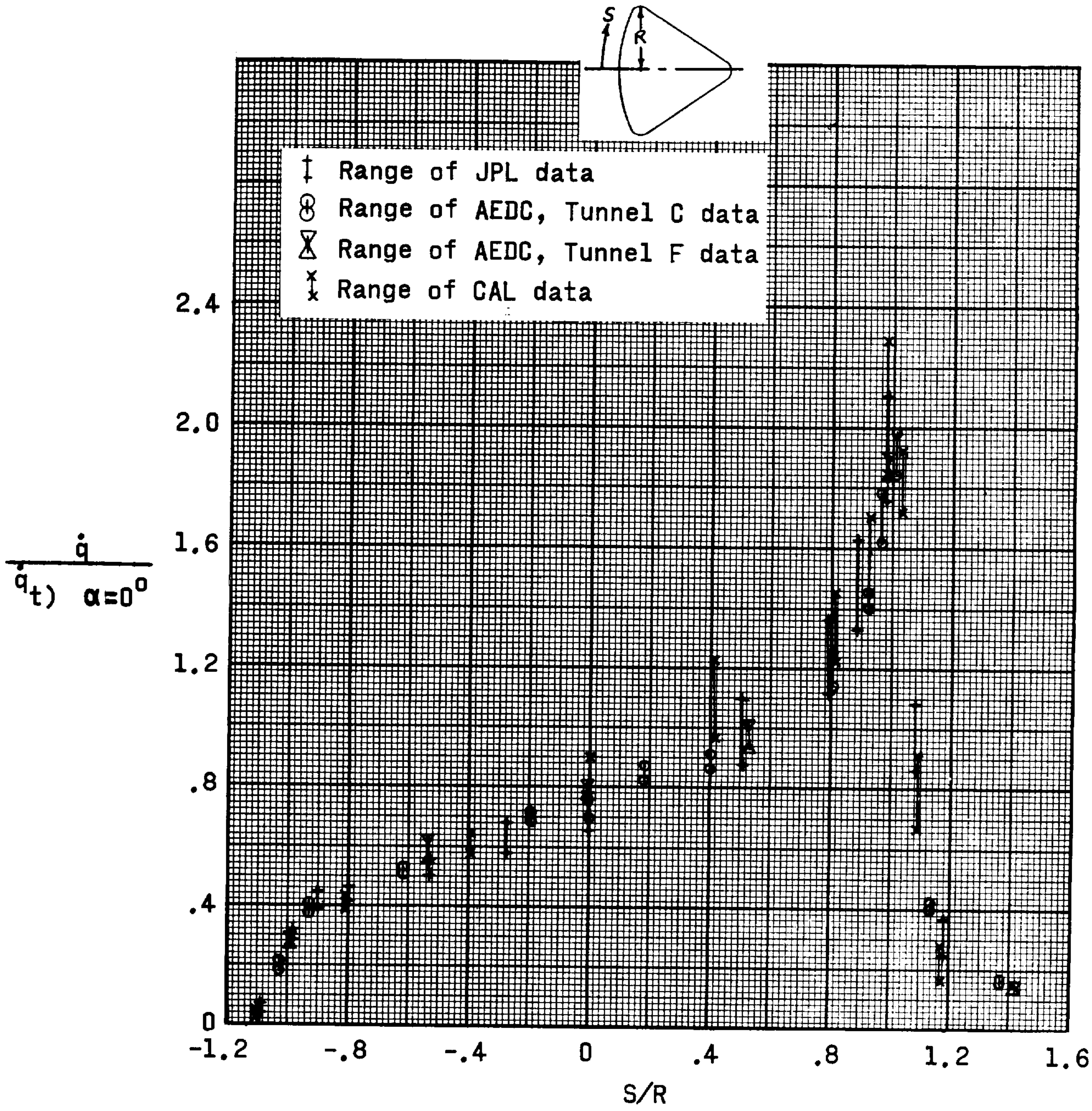

Figure 2.- Laminar heat transfer rate distribution in the pitch plane of the reentry configuration at 33° angle of attack.

[redacted]

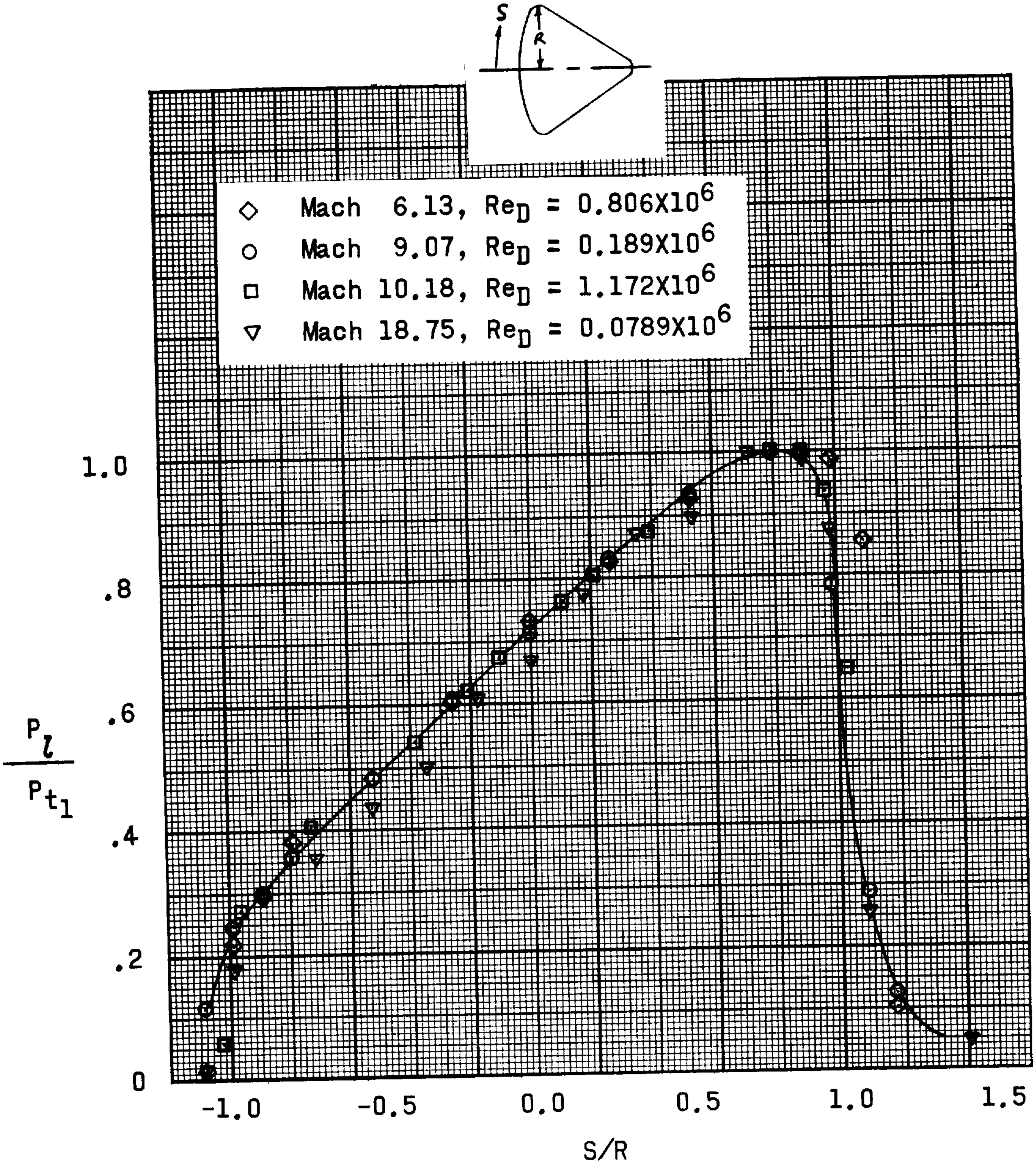

Figure 3.- Experimental pressure distribution in the pitch plane of the entry configuration at 33° angle of attack.

[redacted]

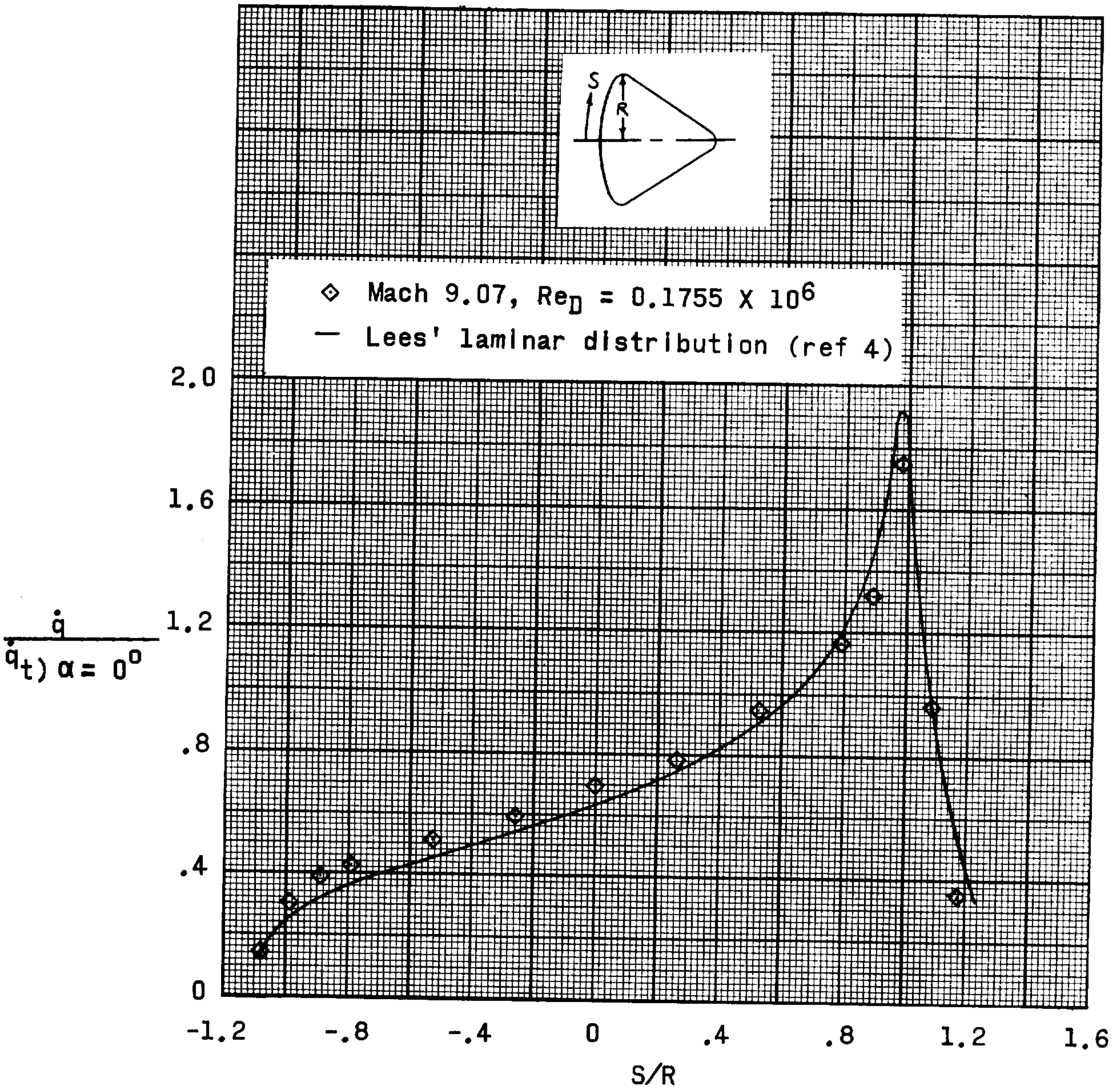

Figure 4.- Comparison of experimental and theoretical heat transfer rate distribution in the pitch plane of the reentry configuration at 33° angle of attack.

[redacted]

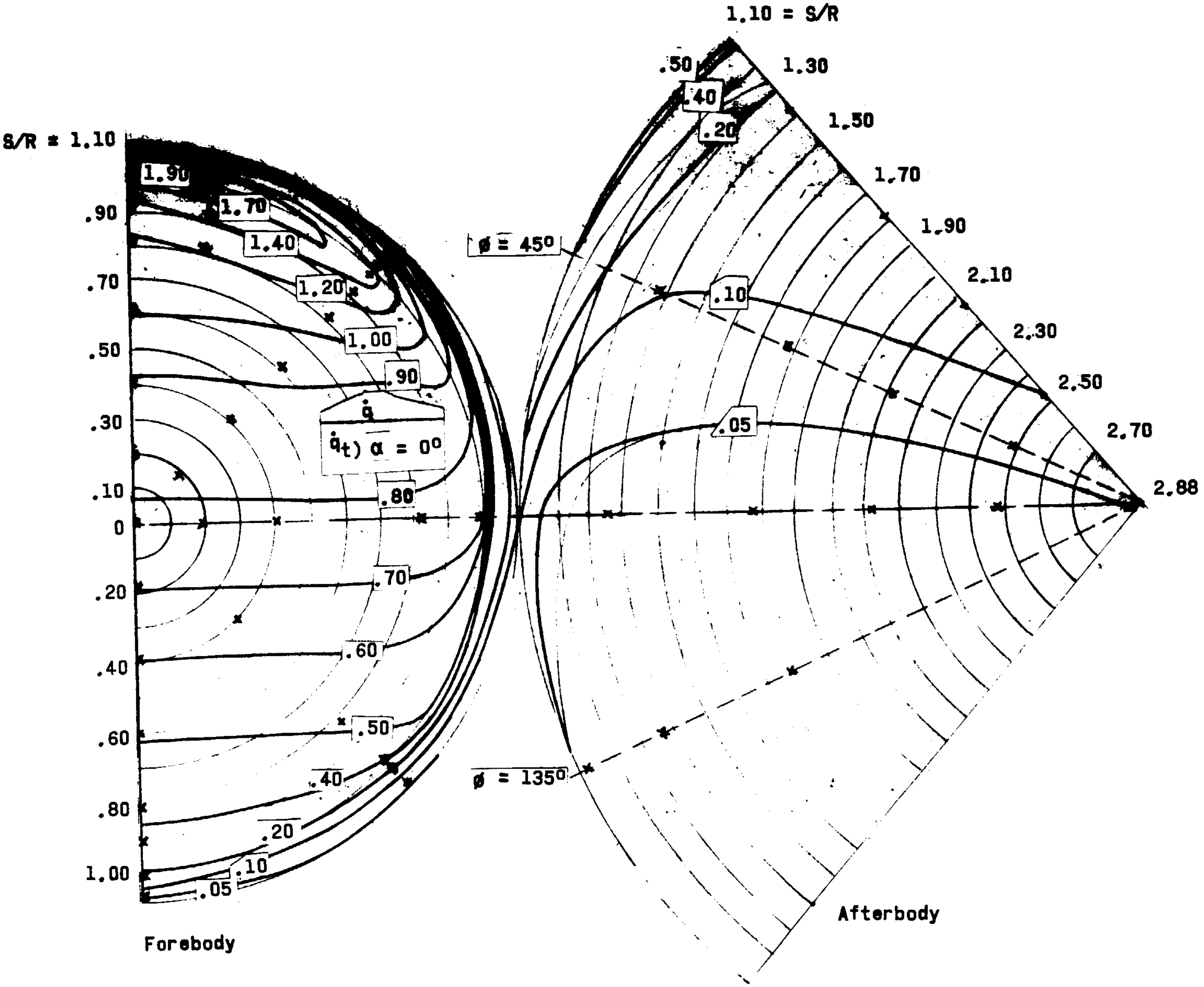

Figure 5.- Heat transfer rate distribution for the reentry configuration at 33° angle of attack.

[redacted]

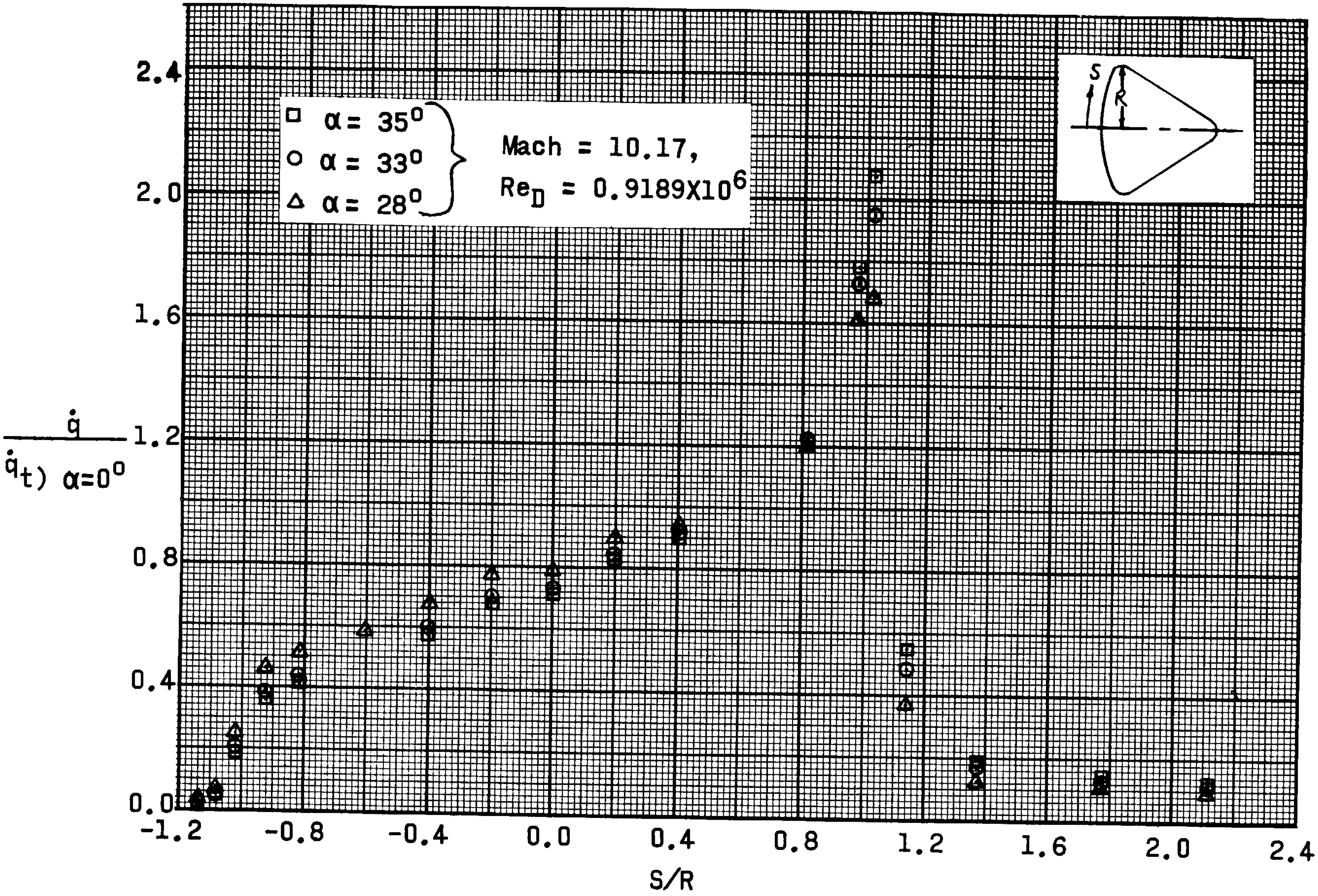

Figure 6.- Heat transfer rate distribution in the pitch plane of the reentry configuration as a function of angle of attack.

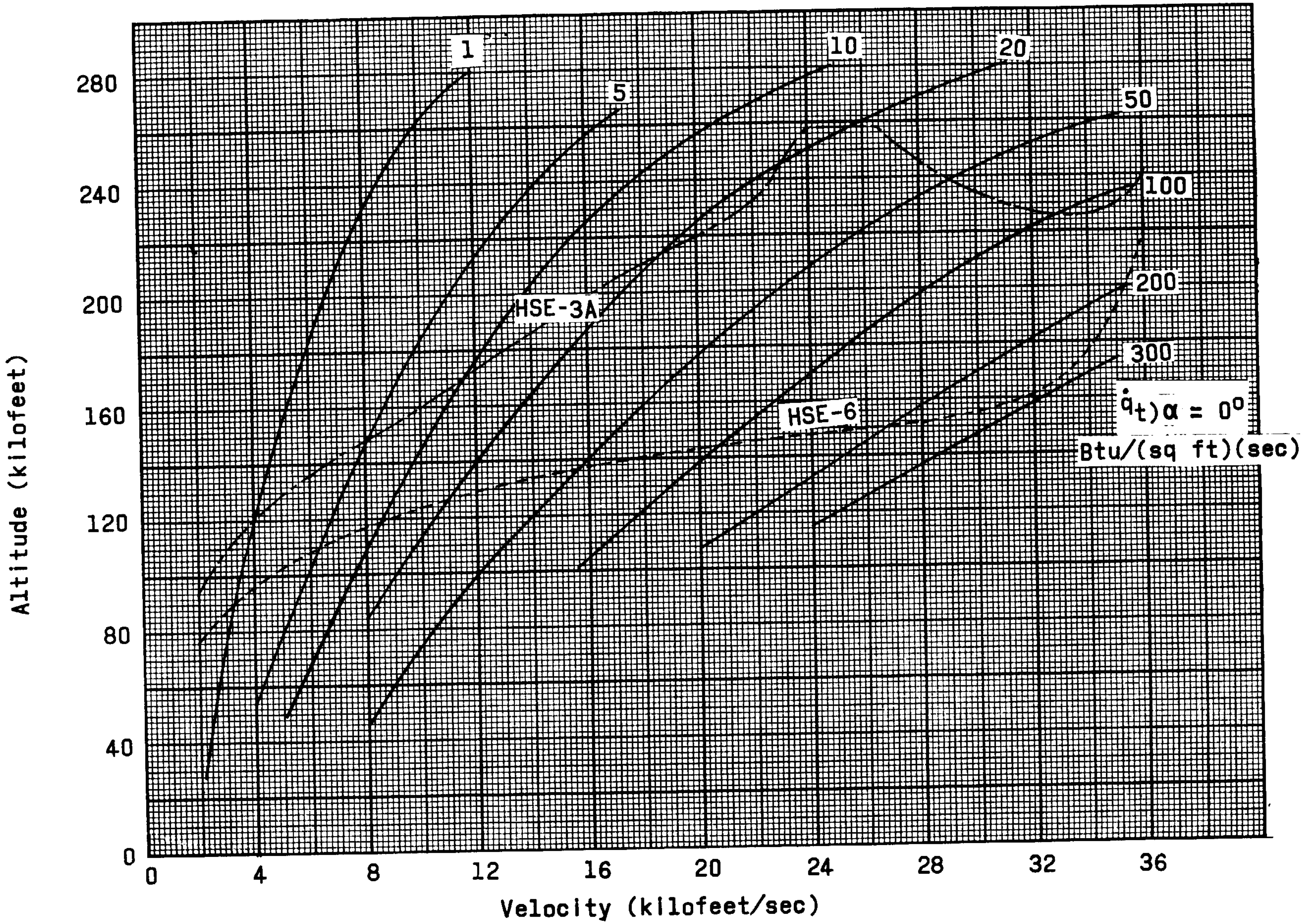

Figure 7.- Convective heat transfer rate at the stagnation point of the reentry configuration at zero angle of attack.

[redacted]

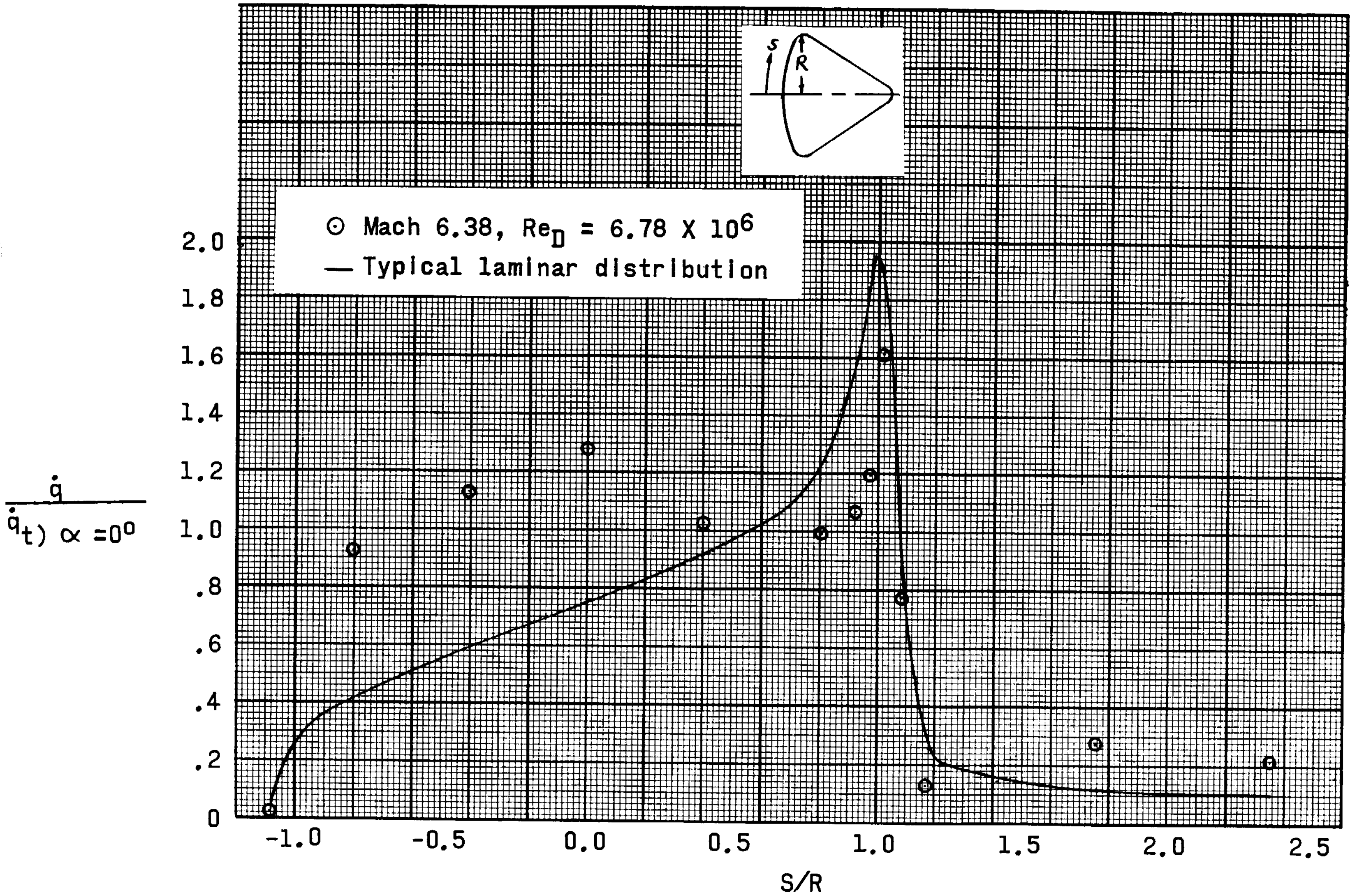

Figure 8.- Heat transfer rate distribution in the pitch plane of the reentry configuration at 33° angle of attack.

[redacted]

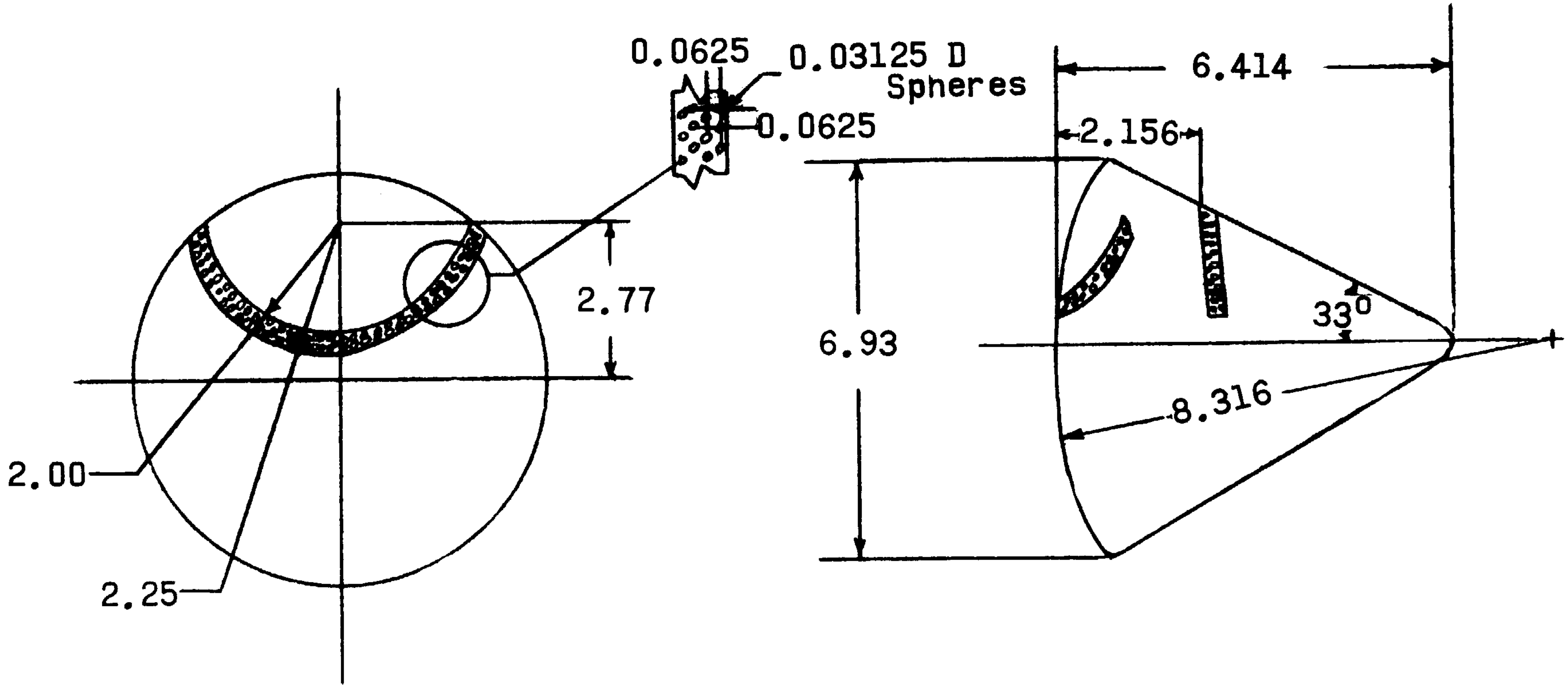
0.0625
0.03125 D
Spheres
0.0625
2.77
2.00
2.25
6.414
2.156
6.93
33°
8.316

Note: All dimensions in inches.

Figure 9.- Boundary layer trip configuration

[redacted]

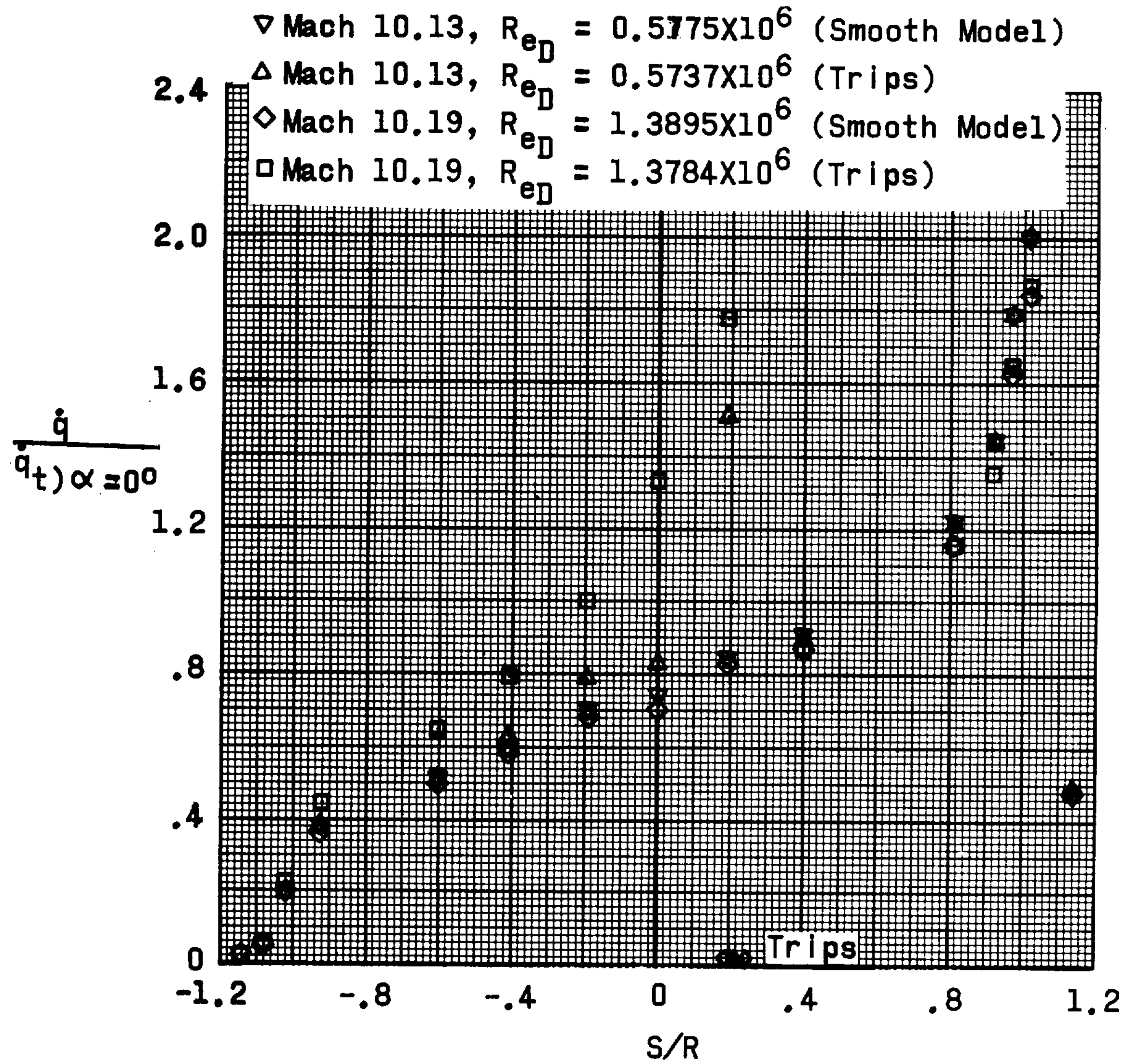

Figure 10.- Comparison of heat transfer rate distribution for the spherical heat shield obtained using models with and without boundary layer trip.

[redacted]

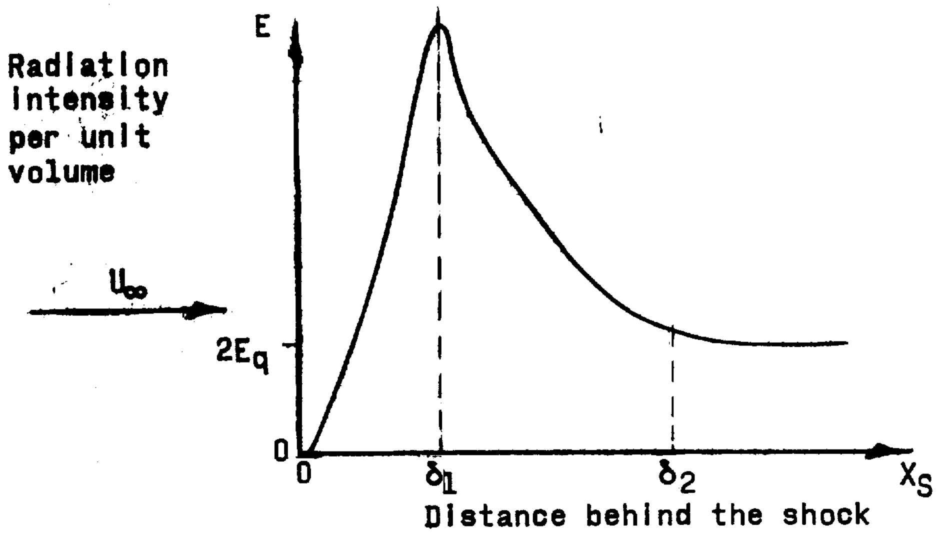

(a) Profile of thermal radiation intensity behind a strong shock in air.

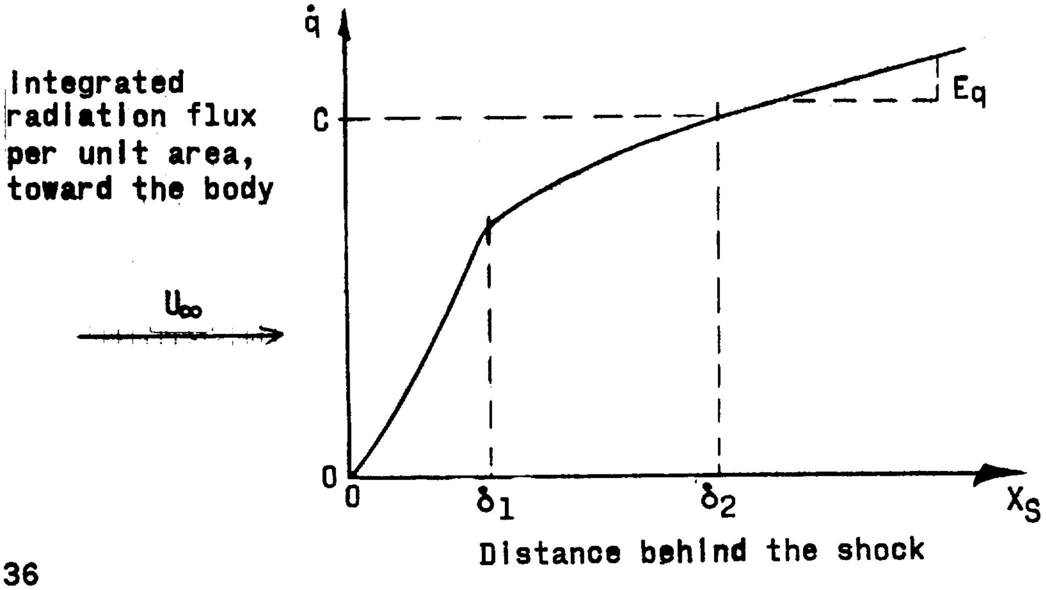

(b) Integrated radiation flux toward the body as a function of the distance behind the shock.

Figure 11.- Thermal radiation characteristics associated with a strong shock in air.

[redacted]

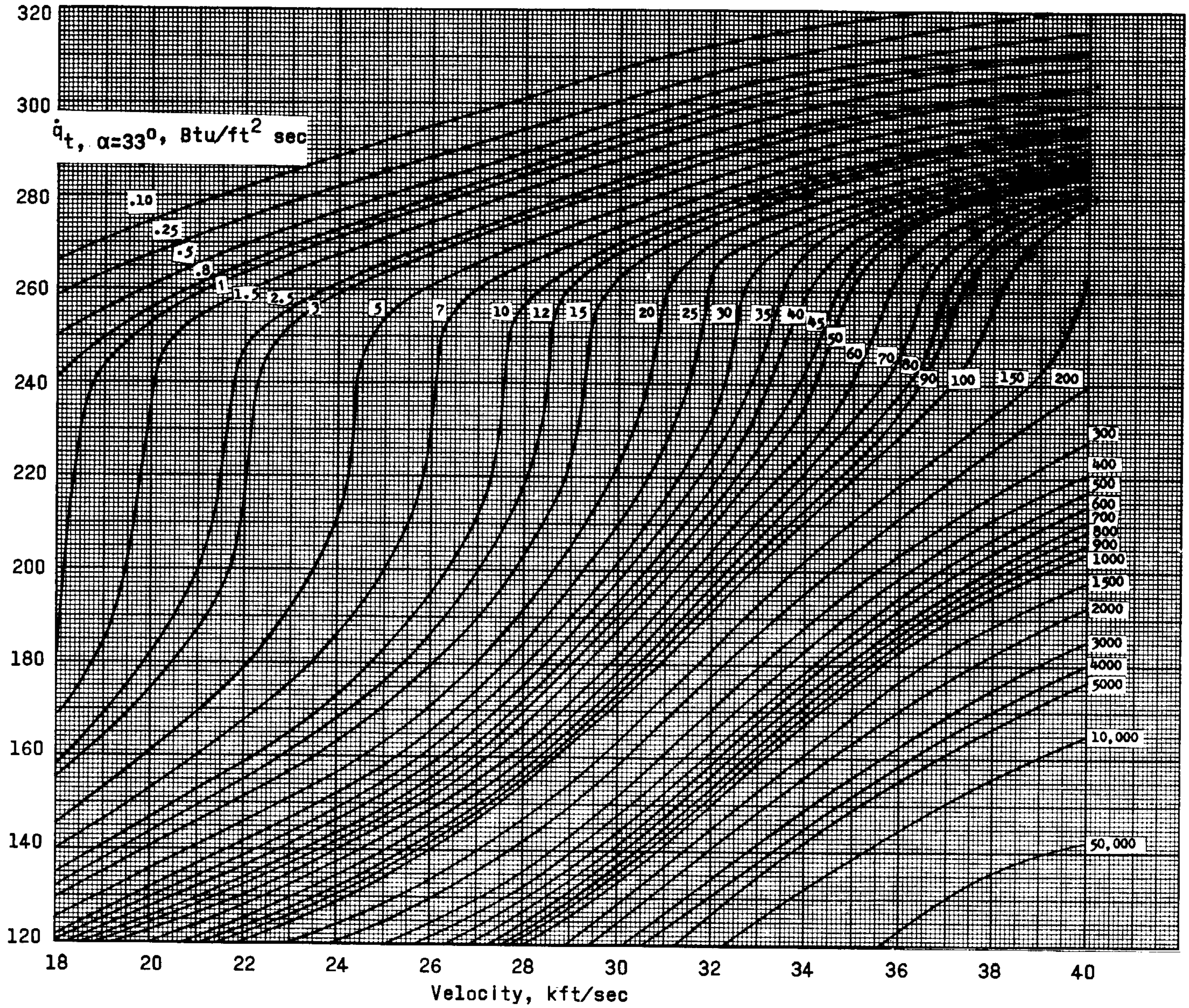

Figure 12.- Thermal radiation flux to the stagnation point of the Apollo at 33° angle of attack.

[redacted]

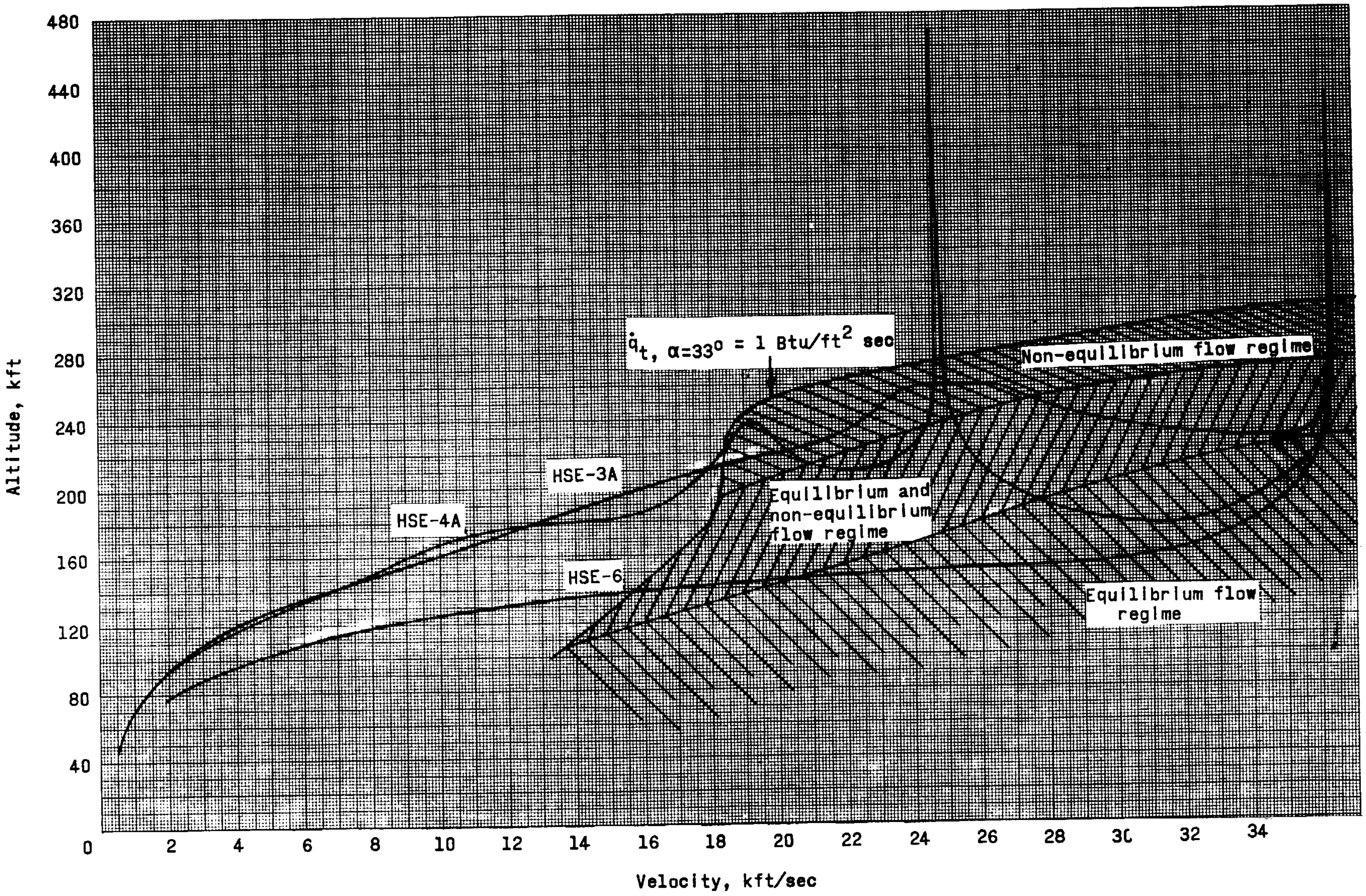

Figure 13.- Flow regimes experienced by the Apollo at angle of attack as a function of the altitude and the velocity.

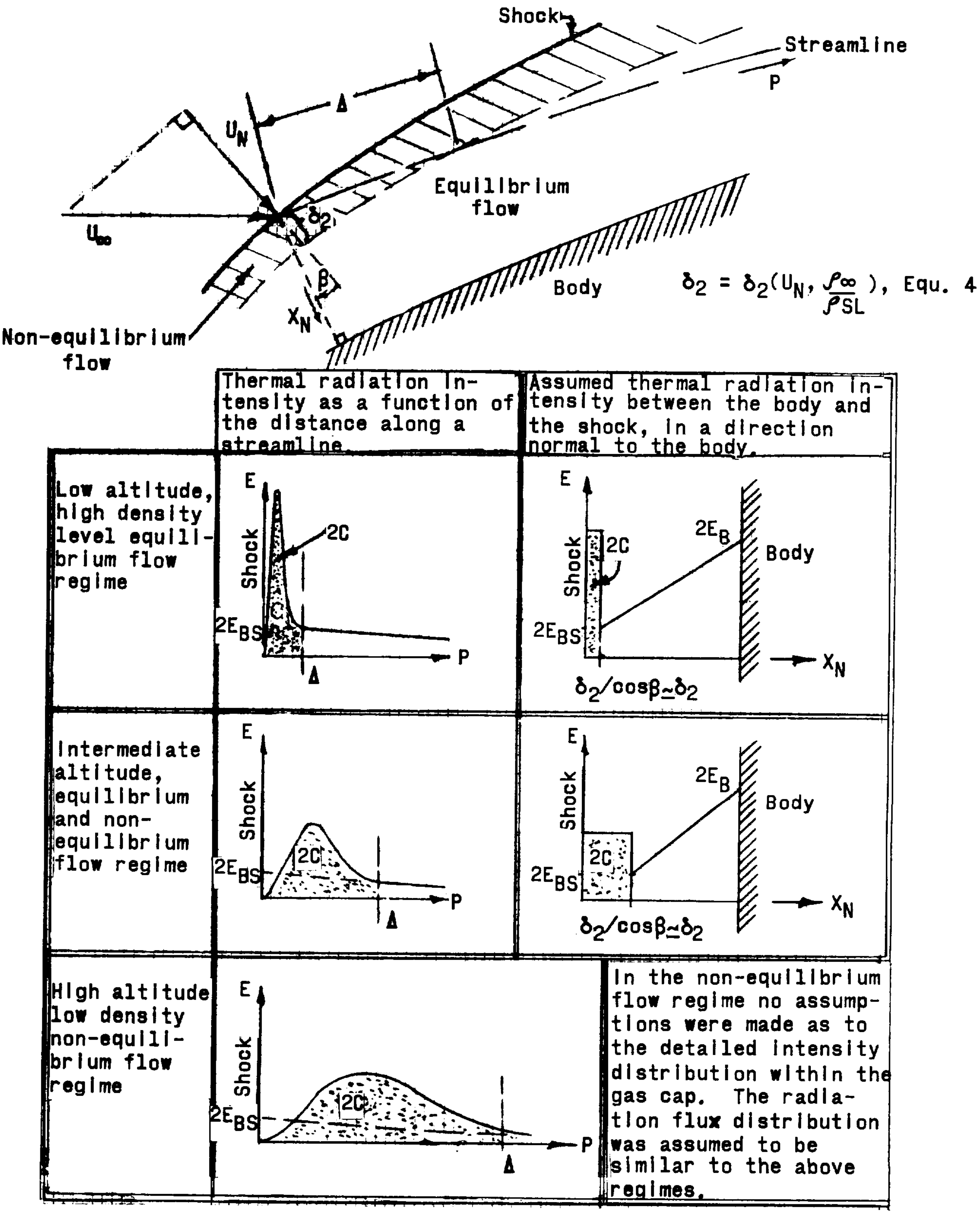
Shock
Streamline
P
Δ
U_N
U_∞
δ_2
Equilibrium flow
β
X_N
Body
Non-equilibrium flow
$\delta_2 = \delta_2(U_N, \frac{\rho_\infty}{\rho_{SL}})$, Equ. 4
E
Shock
2C
$2E_{BS}$
P
Δ
$2E_B$
X_N
$\delta_2/\cos\beta \simeq \delta_2$

Thermal radiation intensity as a function of the distance along a streamline.

Assumed thermal radiation intensity between the body and the shock, in a direction normal to the body.

Low altitude, high density level equilibrium flow regime

Intermediate altitude, equilibrium and non-equilibrium flow regime

High altitude low density non-equilibrium flow regime

In the non-equilibrium flow regime no assumptions were made as to the detailed intensity distribution within the gas cap. The radiation flux distribution was assumed to be similar to the above regimes.

Figure 14.- Schematic representation of the approximations used to obtain the thermal radiation flux to a general point on the forebody of the Apollo at angle of attack.

[redacted]

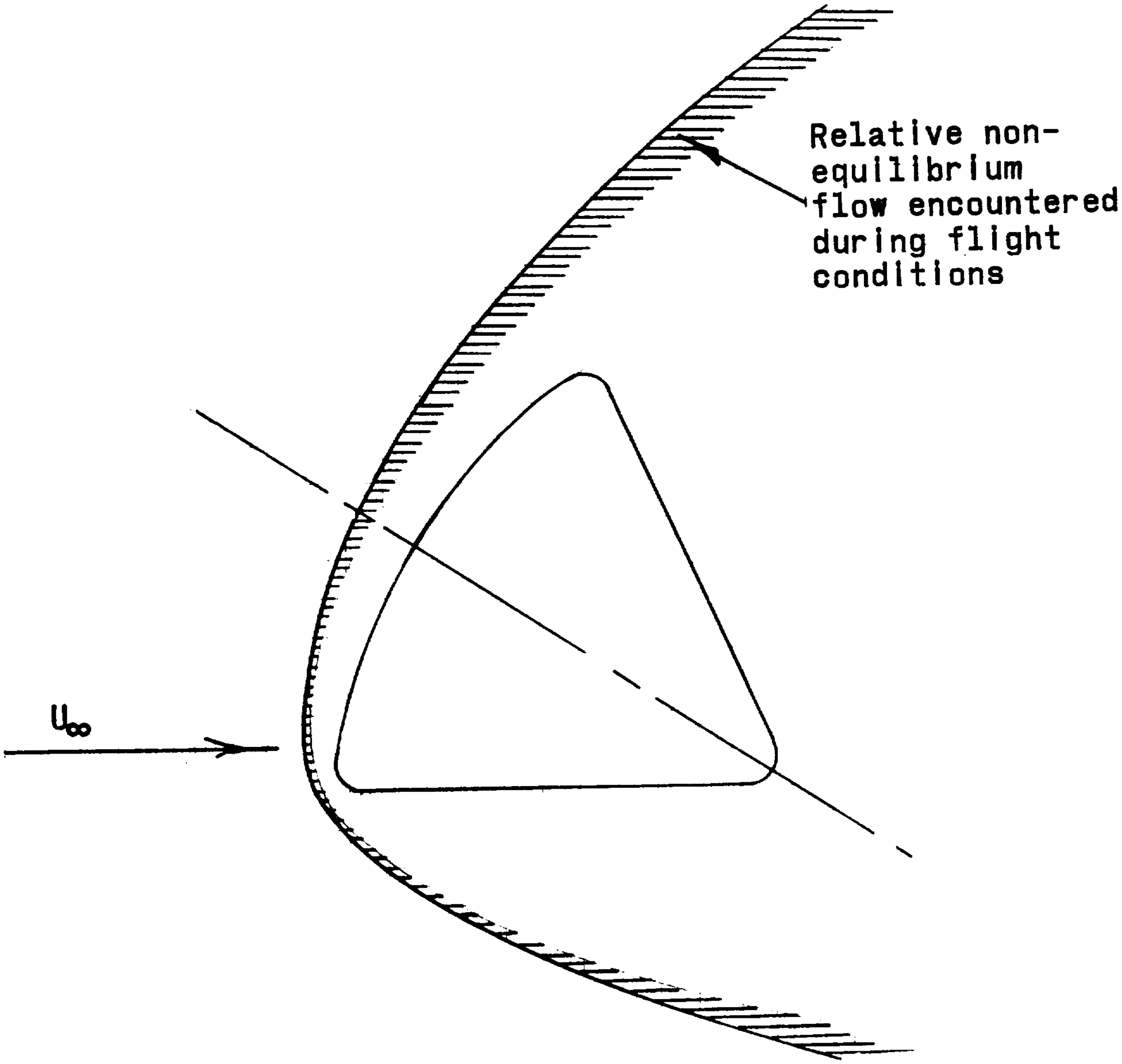
Relative non-equilibrium flow encountered during flight conditions
U_∞

Figure 15.- Schematic representation of the shock shape in the angle of attack plane for the Apollo.

[redacted]

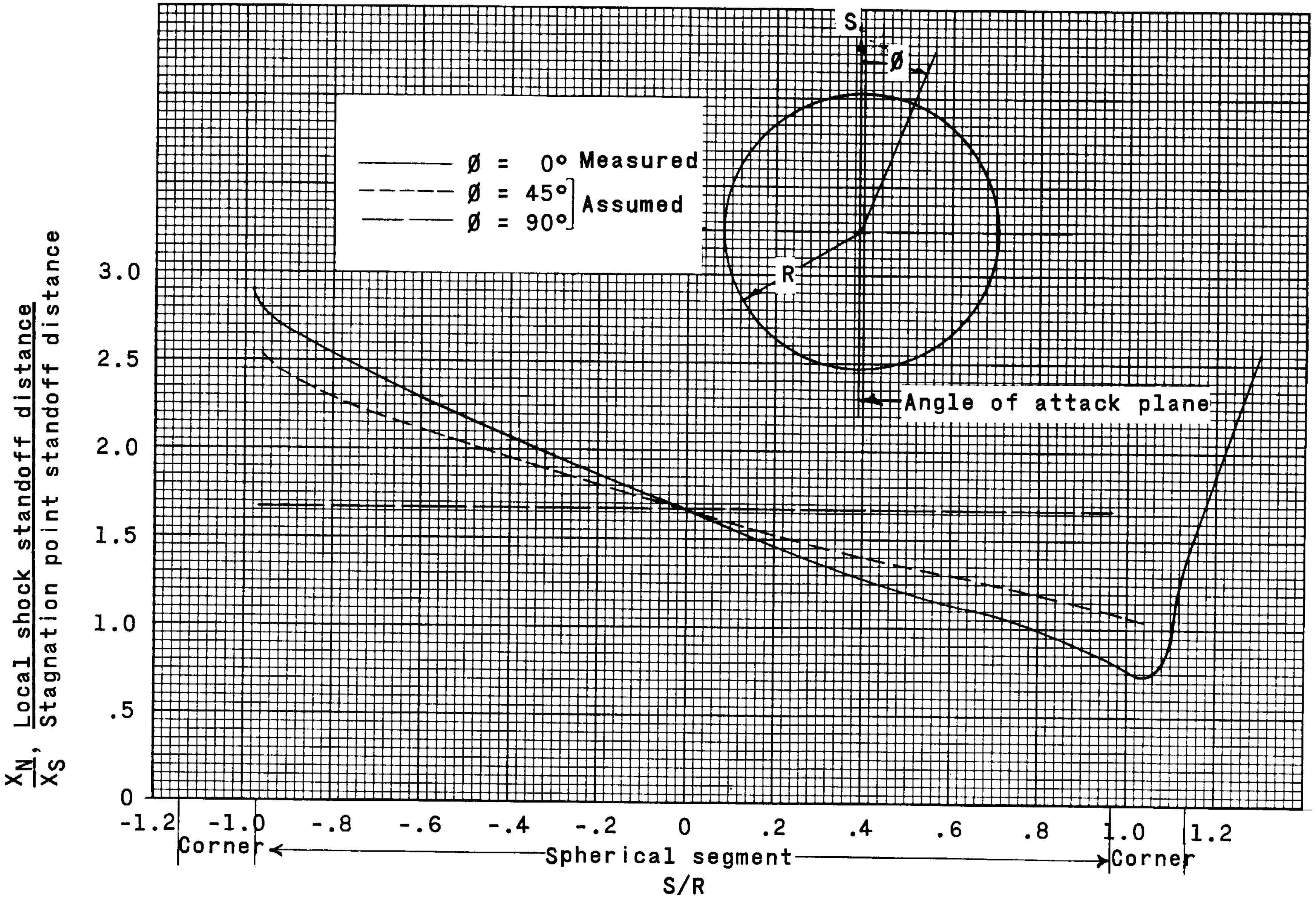

Figure 16.- Measured and assumed relative local shock standoff distance for the forebody of the Apollo at angle of attack.

[redacted]

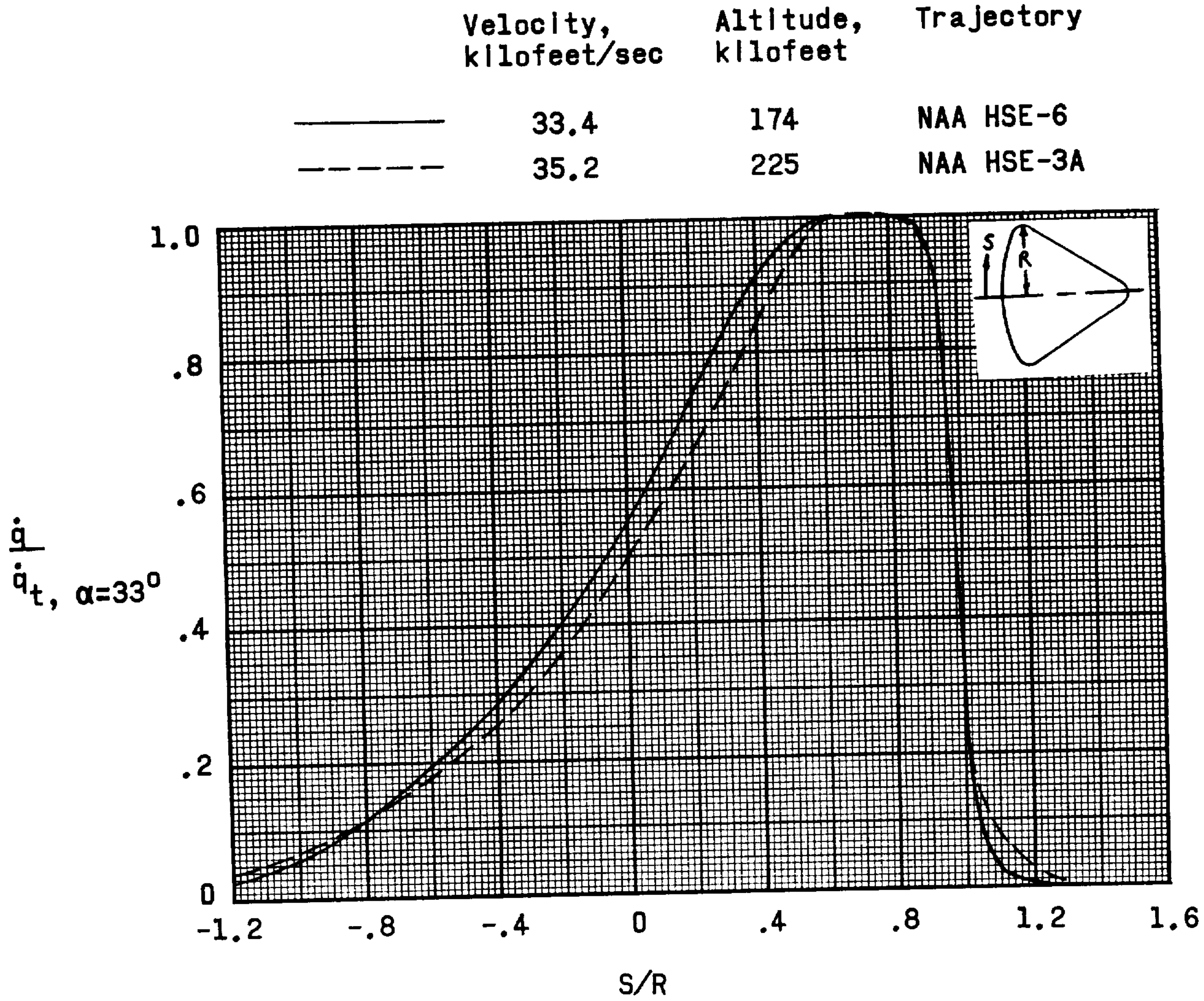

Figure 17.- Relative distribution of thermal radiation flux to the surface of the Apollo at angle of attack.

[redacted]

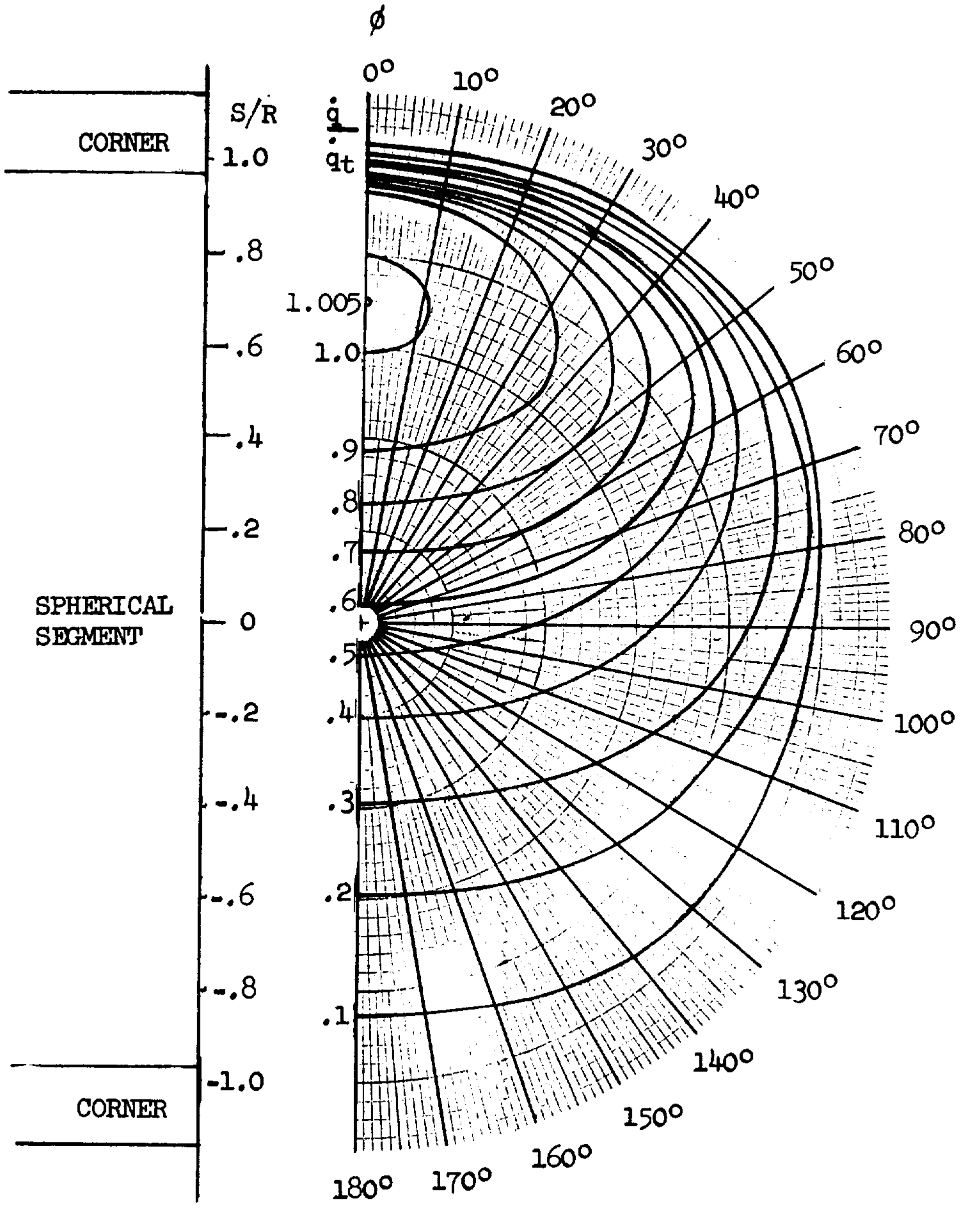

Figure 18.- Distribution of relative thermal radiative heating flux on the forebody of the Apollo at angle of attack.

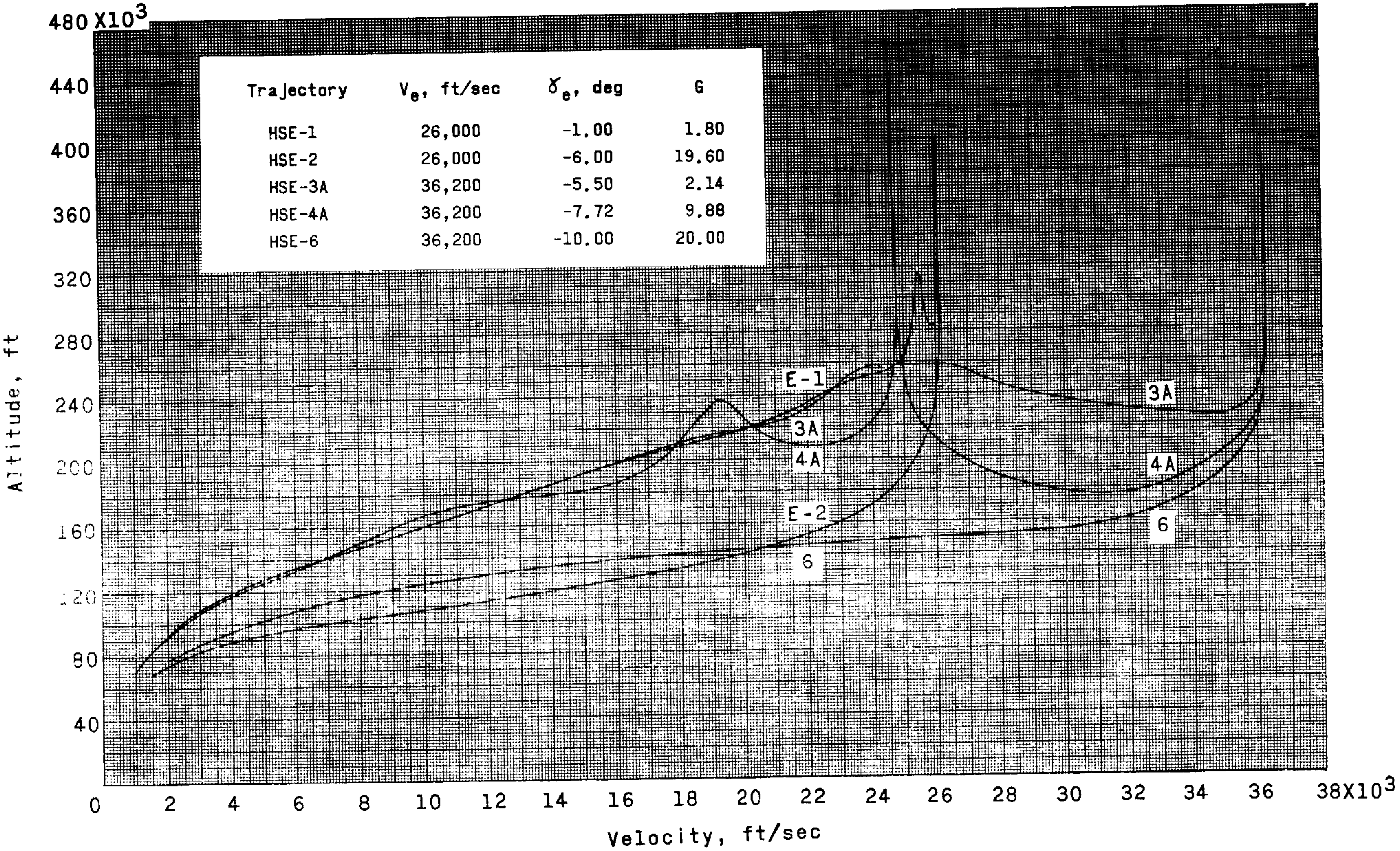

Trajectory	V_e, ft/sec	γ_e, deg	G
HSE-1	26,000	-1.00	1.80
HSE-2	26,000	-6.00	19.60
HSE-3A	36,200	-5.50	2.14
HSE-4A	36,200	-7.72	9.88
HSE-6	36,200	-10.00	20.00

Figure 19.- Heat shield design trajectory envelope.

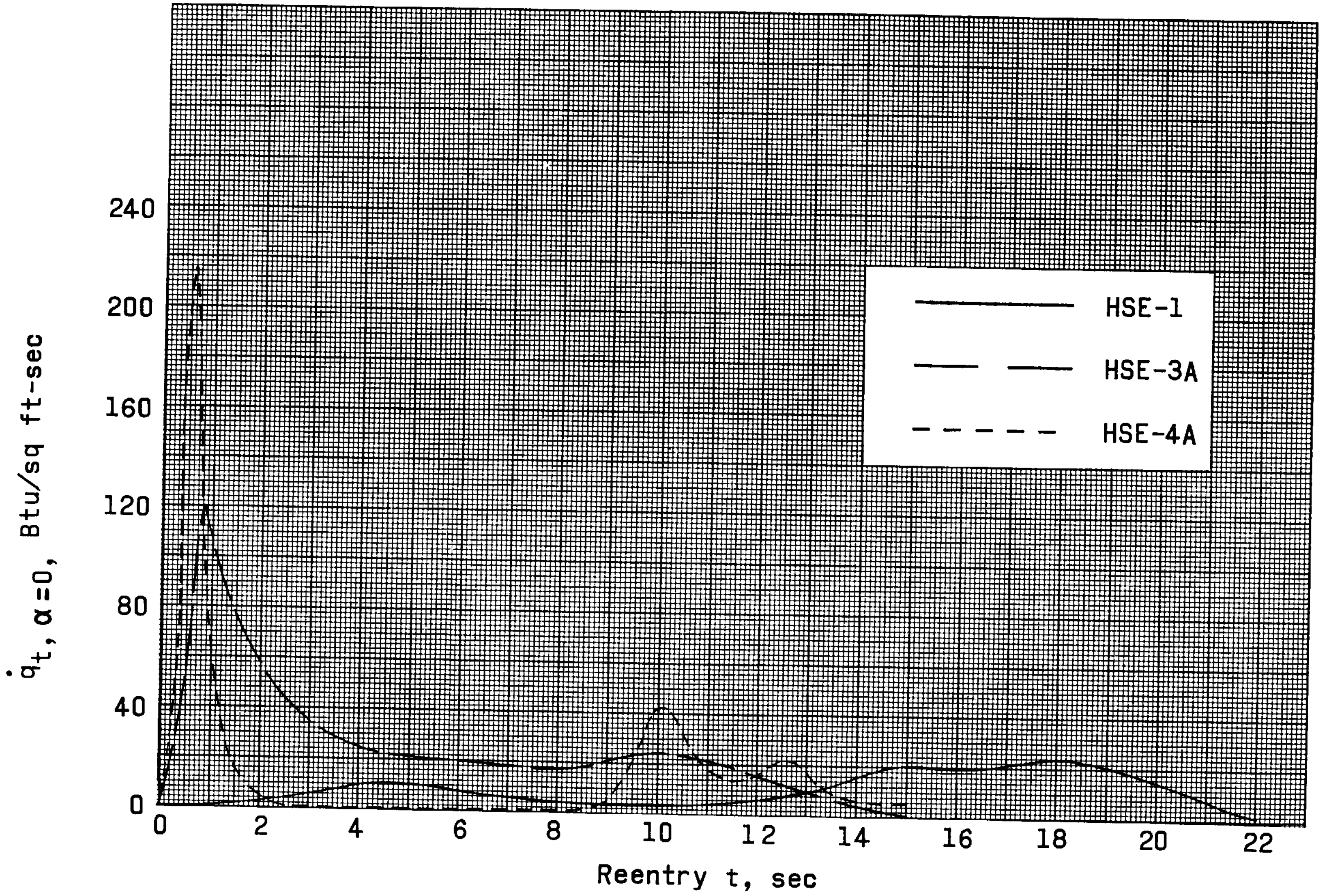

(a) For trajectories HSE-1, HSE-3A, and HSE-4A.

Figure 20.- Time histories of theoretical convective stagnation point heating rates at $\alpha = 0^{\circ}$.

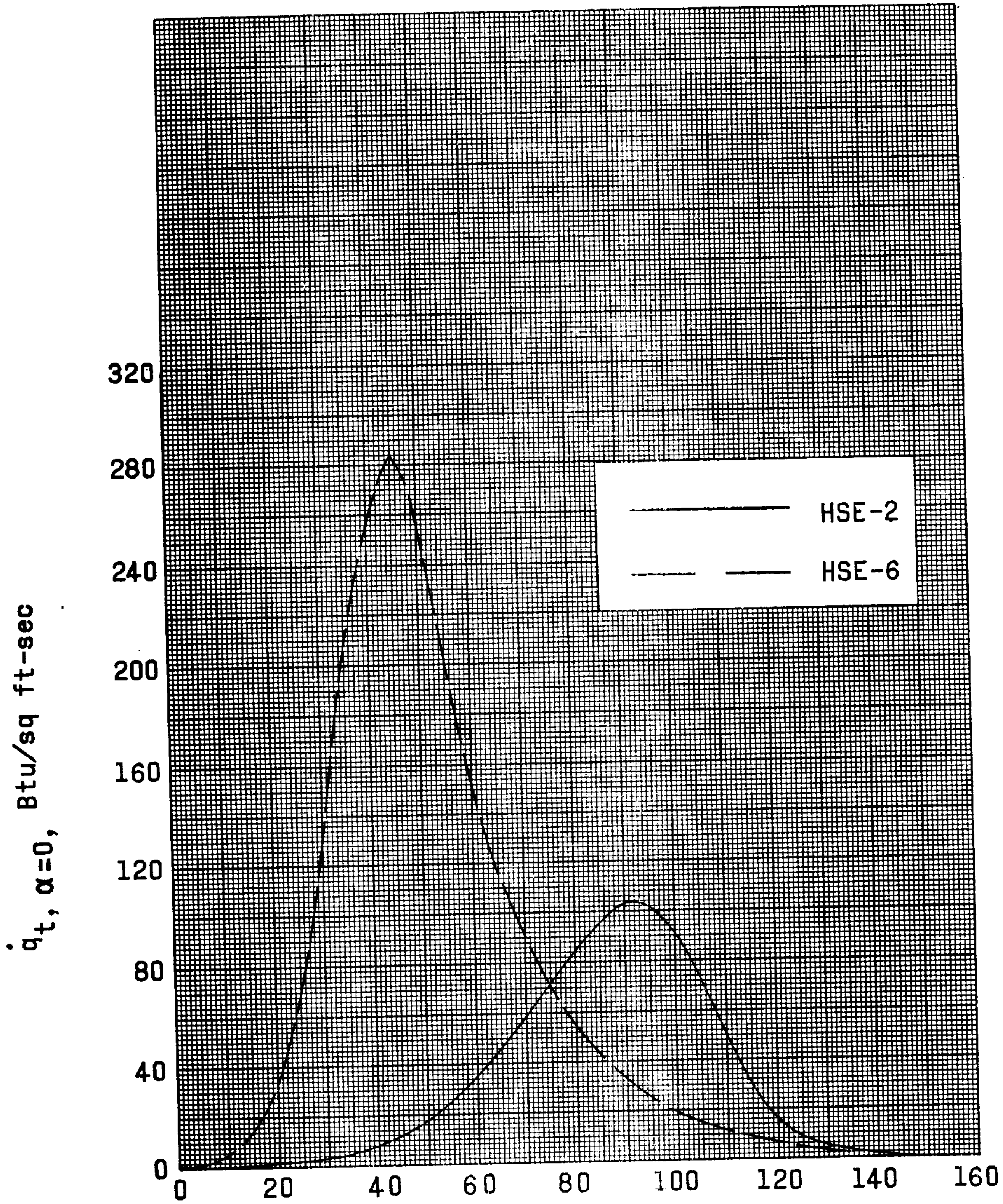

(b) For trajectories HSE-2 and HSE-6.

Figure 20.- Concluded.

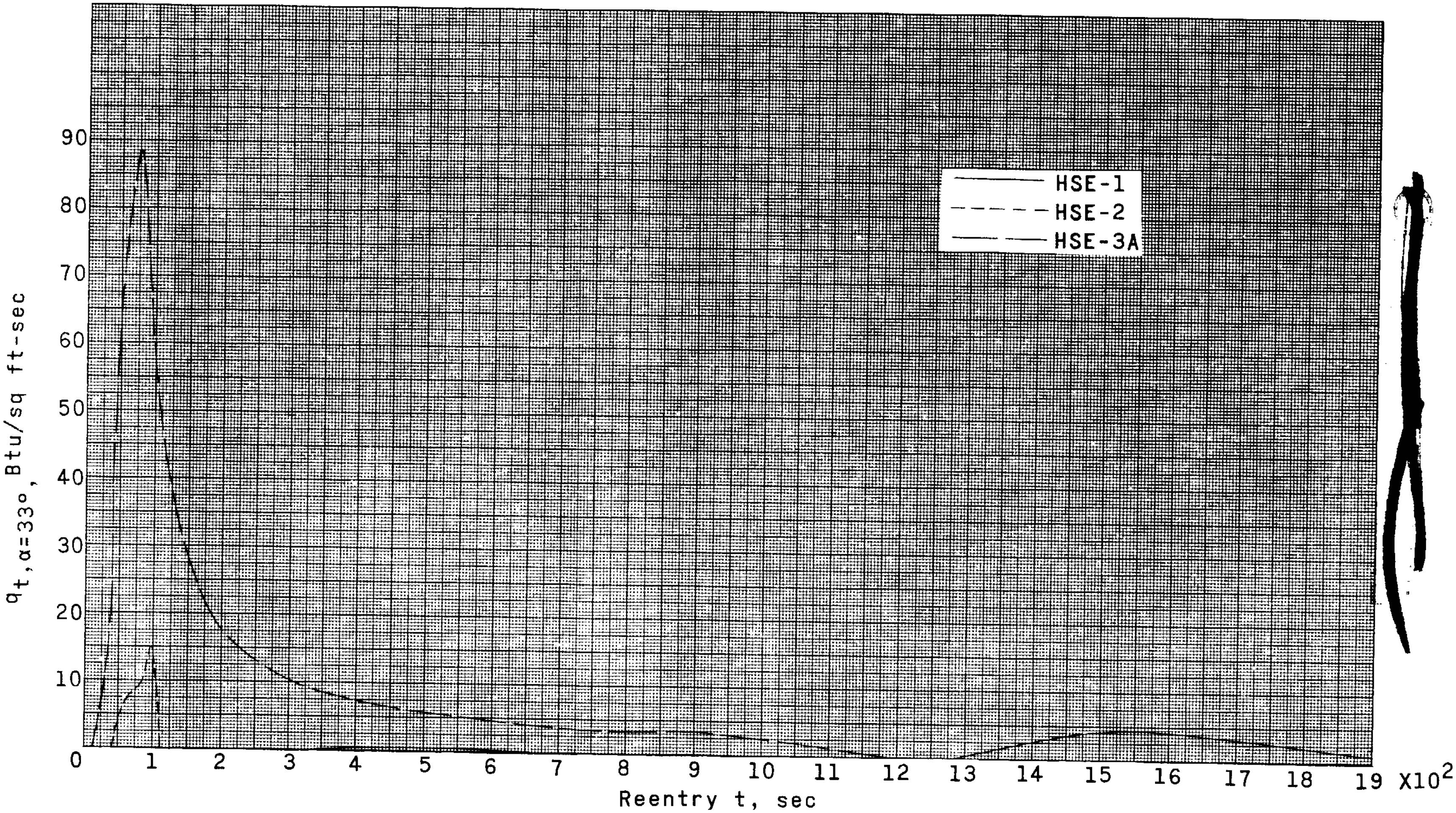

(a) For trajectories HSE-1, HSE-2, and HSE-3A.

Figure 21.- Time histories of theoretical radiative stagnation point heating rates when α=33°.

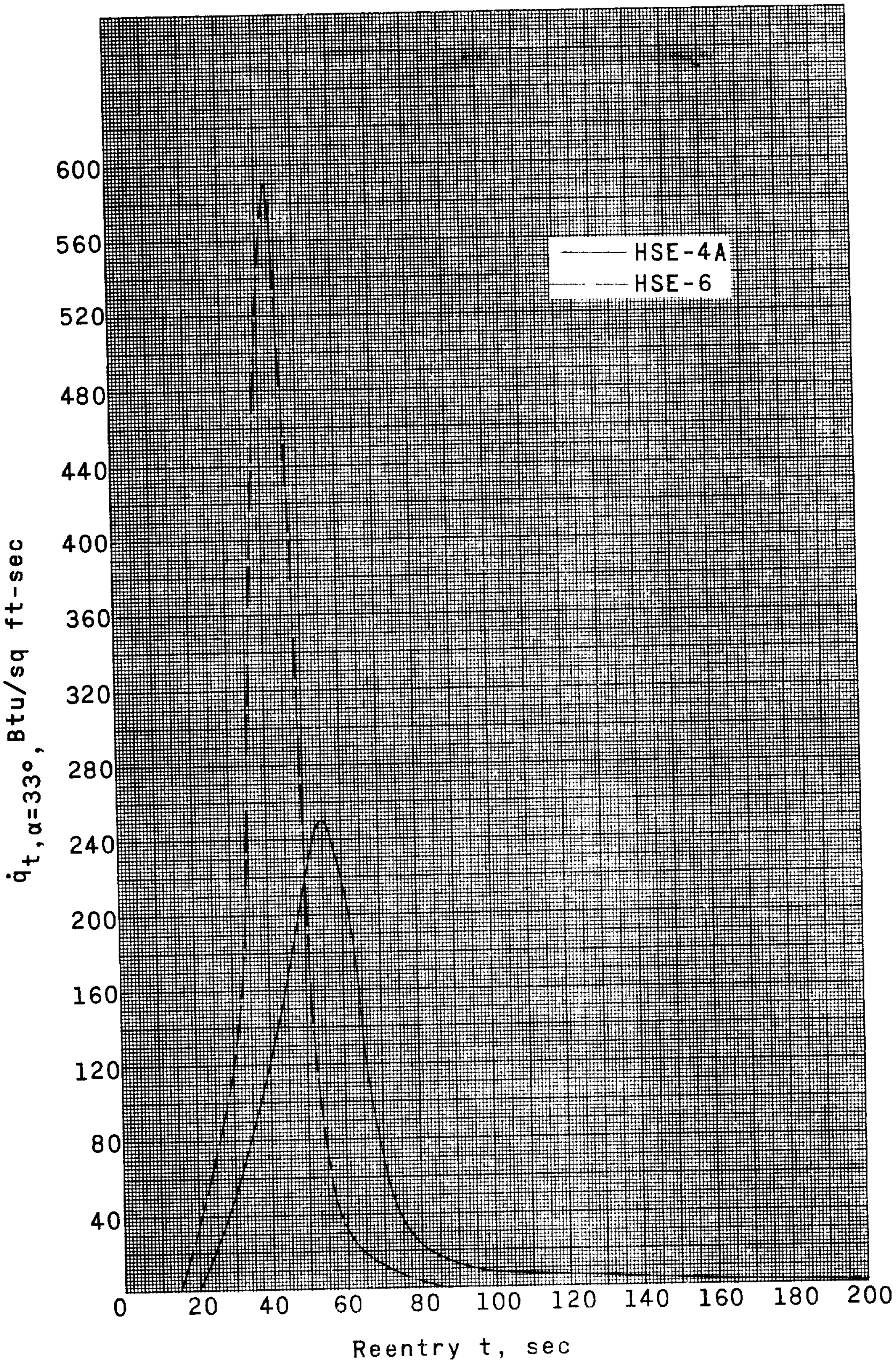

(b) For trajectories HSE-4A and HSE-6.

Figure 21.- Concluded.

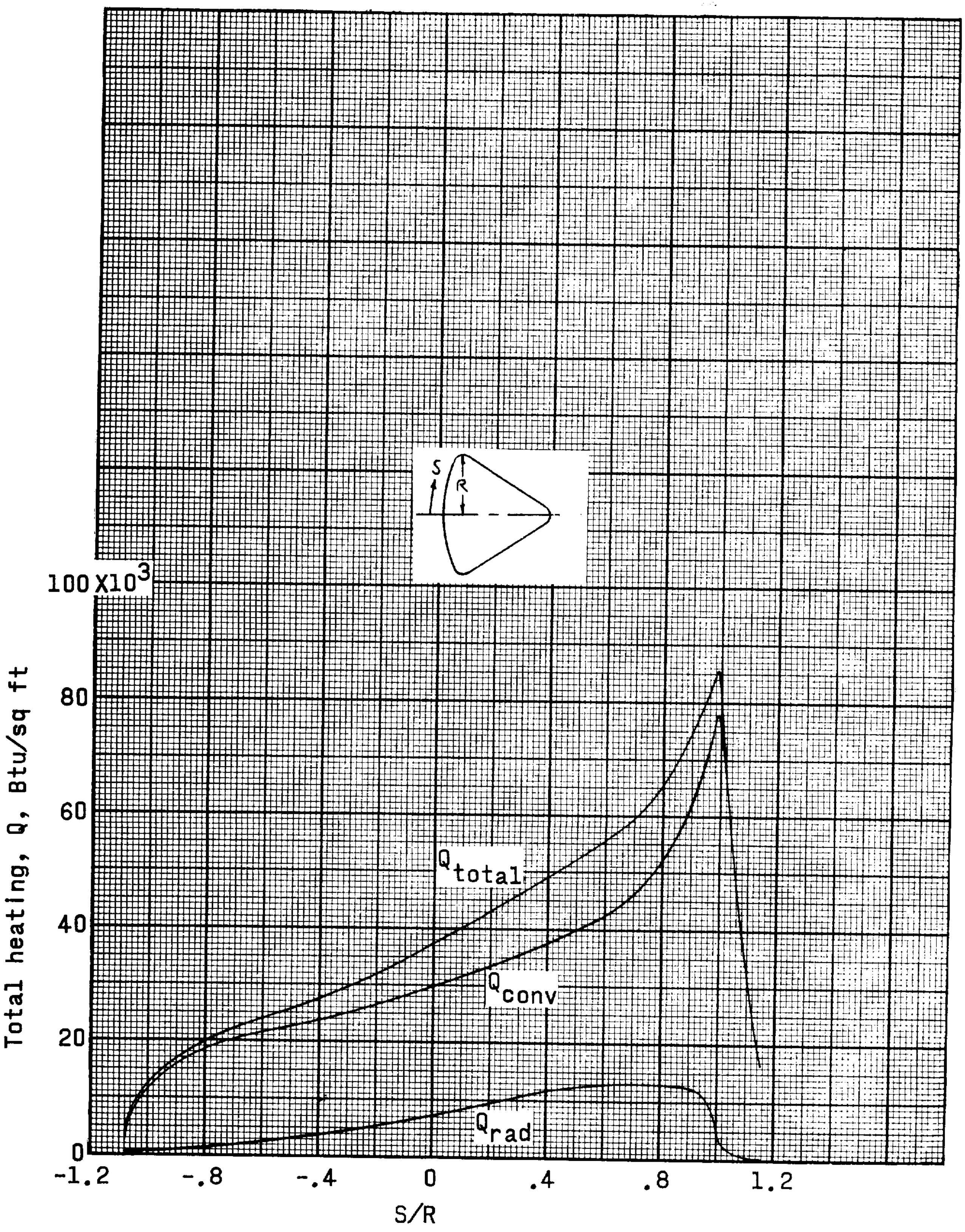

(a) For overshoot trajectory, HSE-3A.

Figure 22.- Distribution of heat load for two design trajectories.

[redacted]

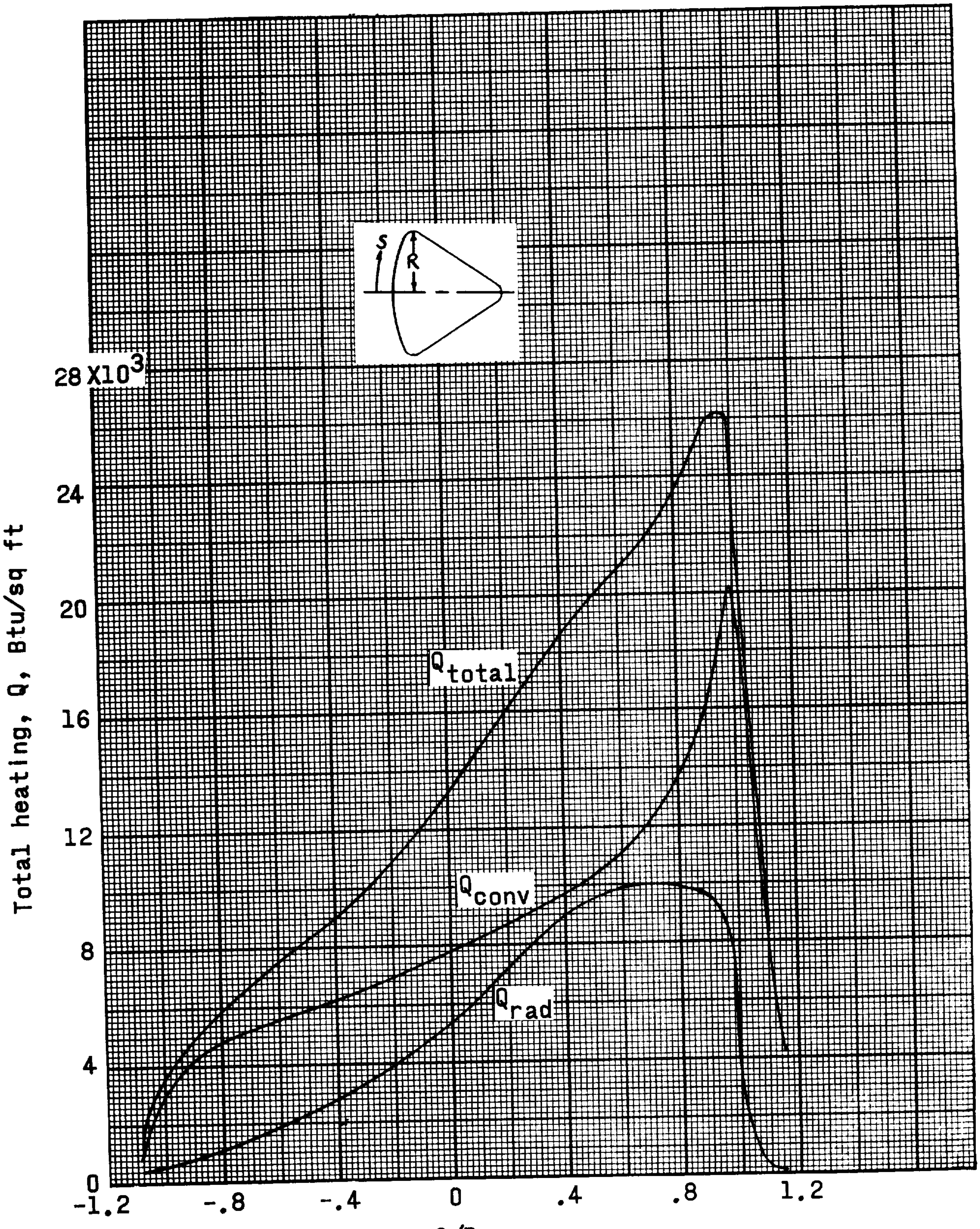

(b) For emergency reentry trajectory HSE-6.

Figure 22.- Concluded.

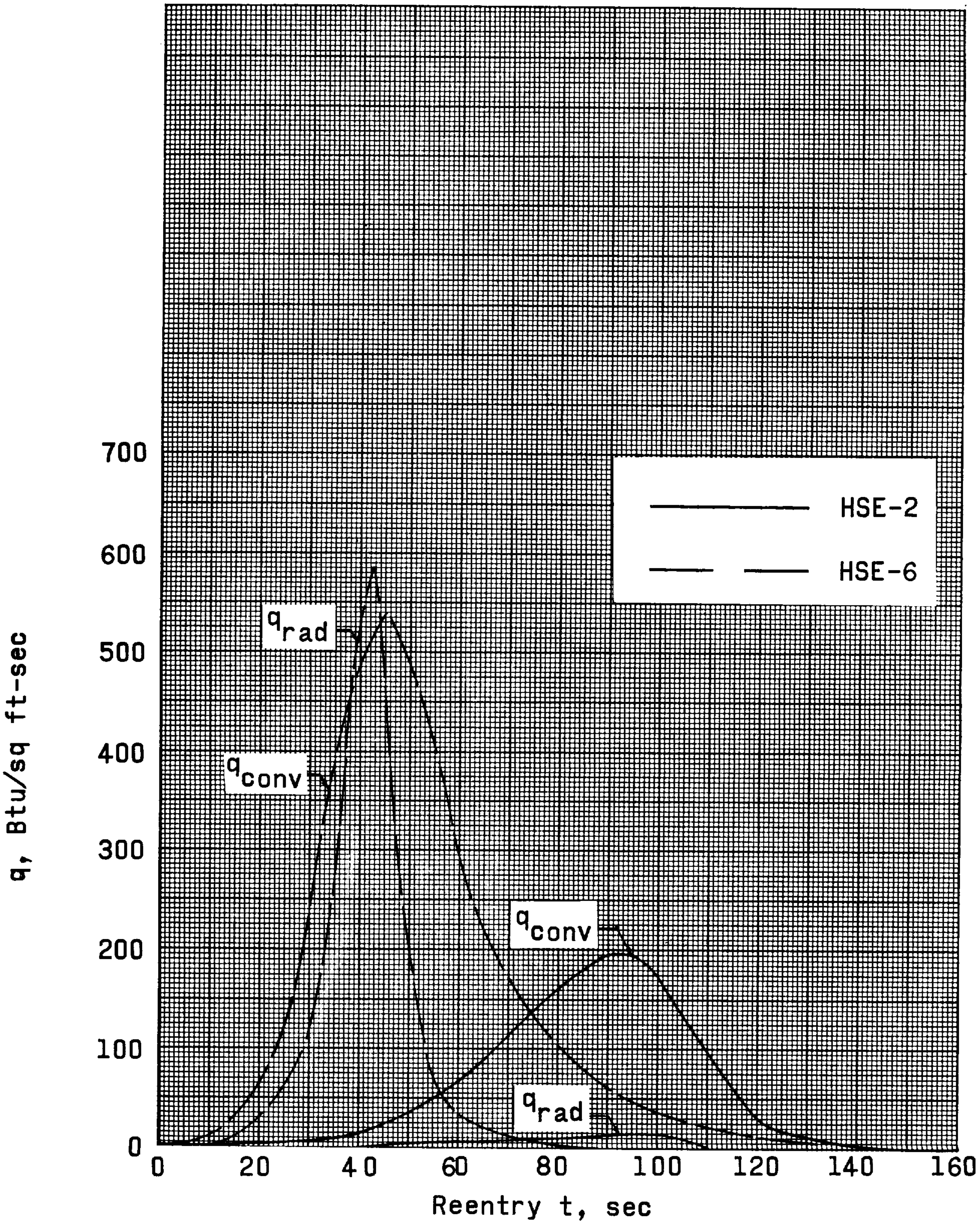

Figure 23.- Heating rates at location of maximum heating.

[redacted]

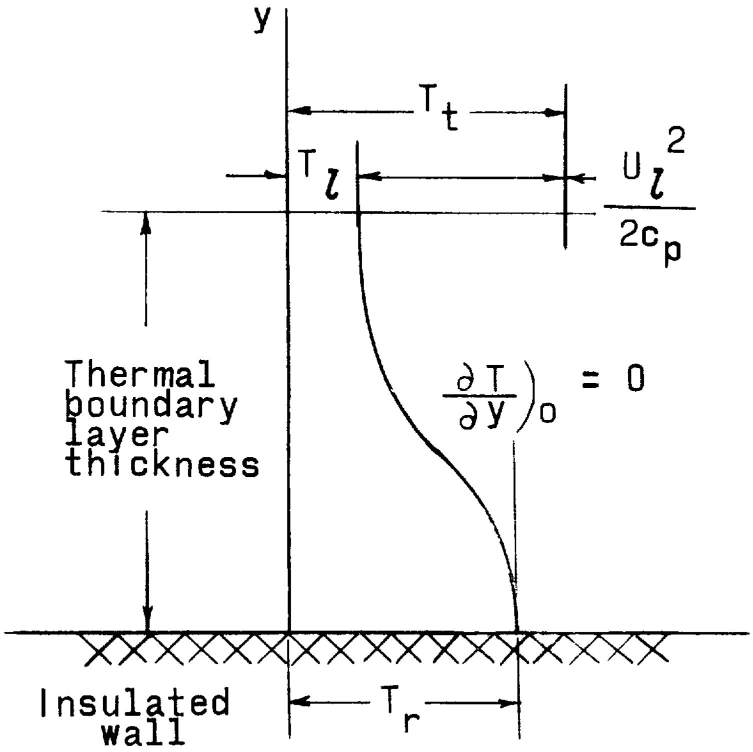
y
T_t
T_l
$\frac{U_l^2}{2c_p}$
Thermal boundary layer thickness
$\left.\frac{\partial T}{\partial y}\right)_0 = 0$
Insulated wall
T_r

Figure 24.- Temperature distribution near insulated wall.

[redacted]

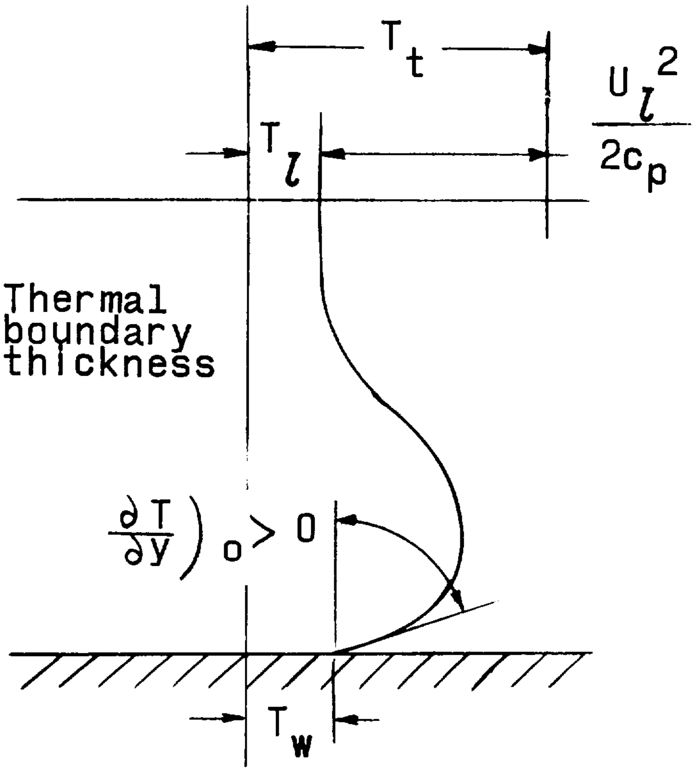
T_t
$\frac{U_l^2}{2c_p}$
T_l
Thermal boundary thickness
$\left.\frac{\partial T}{\partial y}\right)_0 > 0$
T_w

Figure 25.- Temperature distribution near a non-insulated cold wall.

[redacted]